



NTNU – Trondheim
Norwegian University of
Science and Technology

Development of a new class of oxygen ion mixed conductors.

Madelen Mørk Frydenlund

Chemical Engineering and Biotechnology

Submission date: June 2014

Supervisor: Sverre Magnus Selbach, IMTE

Norwegian University of Science and Technology
Department of Materials Science and Engineering

Declaration

This master thesis has been performed at:
Norwegian University of Science and Technology (NTNU)
Department of Material Science and Engineering
Sem Sælandsvei 12 N-7034 Trondheim Norway

Supervisors:

Sverre Magnus Selbach

NTNU Trondheim

Co Supervisors:

Professor Tor Grande

NTNU Trondheim

Ph.D. Candidate Sandra Helen Skjærvø

NTNU Trondheim

M.Sc. Candidate:

Madelen Mørk Frydenlund

I hereby declare that the work in this study has been conducted honestly and independently,
and all used references are denoted.

Trondheim June 20, 2013

Madelen Mørk Frydenlund

Acknowledgements

I would like to take the opportunity to express my gratitude to the extraordinary people that have helped me all the way during my master's thesis.

First, I would thank my supervisor Associated Professor Sverre Magnus Selbach and my co-advisors Sandra Helen Skjærvø and professor Tor Grande for their encouragement, support and for sharing their knowledge on the subject for this thesis.

A special thank you goes to Sverre Magnus Selbach, for his genuine interest on this subject and the time he has set aside every week to have our weekly meetings.

I would also extend my gratitude to everybody participating in the weekly ferrogroupp meetings, and especially thanks to PhD candidate Espen Wefring who always have time to answer my questions.

I also want to thank the technical staff in chemical building K2 for support and knowledge, especially Julian R Tolchard, Pei Na Kui and Gunn Torill Wikdahl.

Finally I want to thank all my friends who have made these five past years in Trondheim the best years of my life.

Abstract

Dense ceramic membranes with mixed ionic and electronic conductivity can separate 100 % pure oxygen from air at elevated temperature. They constitute a much cheaper and more environmentally friendly alternative to cryogenic distillation. Today the challenge with dense ceramic membranes is the long term stability. The high operating temperatures (>800°C) of the membranes lead to chemical degradation and mechanical failure. Hexagonal manganites has the ability to reduce the problems associated with high temperatures. Compared to perovskites, which conduct through formation of oxygen vacancies, hexagonal manganites have the ability to form interstitial oxygen due to a less closed packed structure. In this thesis, it is reported on how the structure and oxygen storage ability changes with varying yttrium deficiency in hexagonal YMnO_3 . It is important to investigate the possibility of cation vacancies in the structure, as little is known about the defect chemistry of these materials. Yttrium deficient samples of YMnO_3 made by solid state synthesis was fired in air, and annealed in varying atmospheres. Hexagonal YMnO_3 has the ability to lose 15-20 % yttrium without any notable changes in the structure and composition of yttrium deficient YMnO_3 . Above this limit, reflections from Mn_3O_4 hausmannite appears in x-ray diffractograms. With a higher degree of yttrium deficiency in the hexagonal structure prepared in air, a slight contraction of the unit cell along both a and c direction is found. After annealing in O_2 atmosphere, the structure expands along the a axis and contracts along the c-axis. The opposite behavior is seen in inert (N_2) atmosphere, where the structure expands in c direction and contract along the a axis with increased yttrium deficiency in YMnO_3 . Above 600 °C, during heating of YMnO_3 and $\text{Y}_{0.80}\text{MnO}_3$, oxygen goes out of the materials in both N_2 and O_2 atmospheres. Upon cooling in O_2 atmosphere, a reversible oxygen uptake is seen around 400 °C for both YMnO_3 and yttrium deficient YMnO_3 . For stoichiometric YMnO_3 the reversible oxygen adsorption is suggested to be attributed to interstitial oxygen, while for stoichiometric yttrium deficient YMnO_3 it is believed to be filling of oxygen vacancies. The reversible oxygen uptake of YMnO_3 was calculated to be $\delta = 0.034$. Moreover, in this thesis it is also reported on the synthesis of an asymmetric membrane consisting of 15 % titanium substituted YMnO_3 . The asymmetric membrane did not yield a dense functional layer of nanocrystalline $\text{YMn}_{0.85}\text{Ti}_{0.15}\text{O}_3$ on top of the porous support after sintering.

Sammendrag

Keramiske membraner for oksygen separasjon basert på en blanding av ionisk og elektronisk ledende oksid, er billigere og mer miljøvennlig enn kryogenisk destillasjon for produksjon av 100 % rent oksygen. En utfordring som er knyttet til dagens keramiske membraner er kjemisk degradering og redusert levetid som følge av de høye arbeidstemperaturene over 800 °C. I forhold til perovskitter, som brukes mye som materialet i keramiske membraner i dag, har heksagonale manganitter muligheter for å romme interstitielt oksygen og dermed være ionisk ledende ved mye lavere temperaturer. I denne oppgaven rapporteres det om hvordan strukturen og muligheten for oksygen lagring endres med yttrium underskudd i heksagonal $YMnO_3$. Det er lite man vet om defekt kjemien i heksagonale manganitter, og det er derfor her forsket på kation vakanser i $YMnO_3$ for å finne ut mer om dette. Pulver med varierende yttrium underskudd i $YMnO_3$ har blitt laget med fast stoff syntese, brent i luft, og videre varmebehandlet i forskjellige atmosfærer. Hexagonal $YMnO_3$ har muligheten for å miste 15-20 % yttrium uten noen spesielle endringer i strukturen. Over denne grensen, kommer refleksjoner av en Mn_3O_4 fase opp i røntgen diffraktogrammene med økende yttrium underskudd i $YMnO_3$. En liten kontraksjon av strukturen både langs a og c akse er funnet for yttrium underskudds prøver brent i luft. I oksiderende atmosfære (O_2) blir strukturen ekspandert langs a-aksen, men kontraherer langs c-aksen, og i inert atmosfære (N_2) skjer den motsatte med økende yttrium underskudd i $YMnO_3$ ved at c-aksen ekspanderer mens a-aksen kontraherer. Ved oppvarming av heksagonal $YMnO_3$ og $Y_{0.80}MnO_3$ i både oksiderende og inert atmosfære går oksygen ut av materialet ved omtrent 600 °C. Ved avkjøling i oksiderende atmosfære er det et reversibelt oksygen opptak rundt 400 °C for både $YMnO_3$ og $Y_{0.80}MnO_3$. Denne reversible adsorpsjonen av oksygen er trodd til å ha en sammenheng med oksygen vakanser i $Y_{0.80}MnO_3$ og interstitielt oksygen i $YMnO_3$. Oksygen opptaket under avkjøling er beregnet til å være $\delta = 0.034$ for $YMnO_3$ i oksiderende atmosfære. I tillegg har det i denne oppgaven blitt laget en asymmetrisk membran av 15 % titan dopet heksagonal $YMnO_3$. Et tett funksjonelt lag bestående av sintrede nano-partikler av $YMn_{0.85}Ti_{0.15}O_3$ ble ikke oppnådd på en porøs bærer.

List of abbreviations

XRD	X-Ray Diffractometry
SEM	Scanning Electron Microscope
SE	Secondary Electrons
BSE	Back Scatter Electrons
MIEC	Mixed Ionic and Electronic Conductor
TGA	ThermoGravimetric Analysis
HS	High Spin
HTXRD	High Temperature X-ray Diffraction
CN	Coordination Number
TEM	Transmission Electron Microscope
VESTA	Visualizing for Electron and Structural Analysis (software)

Contents

1. Introduction	1
1.1 MIEC membranes.....	2
1.1.1 Material requirements.....	4
1.2 Research objectives	5
2. Literature survey on YMnO_3	7
2.1 Crystal structure	7
2.2 Phase stability.....	9
2.2.1 Crystal field stabilization.....	11
2.3 Thermal and chemical expansion of the structure in varying atmospheres.....	11
2.3.1 Microcracking as a result of anisotropic expansion	13
2.3.2 Substitution with titanium in YMnO_3	14
2.4 Oxygen non-stoichiometry and defect chemistry of YMnO_3	14
2.4.1 Point defects	14
2.4.2 Electronic defects	16
2.5 Theory on synthesis methods	17
2.5.1 Sol gel synthesis	17
2.5.2 Solid state synthesis.....	17
2.5.3 Solid state sintering	18
3. Experimental	19
3.1 Preparation of powders and sintered samples	19
3.1.1 Solid State synthesis of crystalline powder	19
3.1.2 Preparation of the active layer – citric acid method	21
3.1.3 Deposition of the active layer by dip coating	23
3.2 Characterization of the powder	23
3.2.1 Structure and composition by x-ray diffraction.....	23
3.2.2 Structure and composition analysis by Rietveld and Pawley method.	23
3.2.3 Microstructure	25
3.3 Affect by atmosphere on unit cell parameters in yttrium deficient YMnO_3	25
3.4 Mass change in YMnO_3 and $\text{Y}_{0.80}\text{MnO}_3$ in varying atmosphere	26
4. Results	27
4.1 Structure and characterization of YMnO_3 and yttrium deficient YMnO_3 powder	27
4.1.1 Structural analysis of $\text{Y}_{1+x}\text{MnO}_3$ by x-ray diffraction and refined unit cell parameters by Pawley method	27
4.2 Mass change of YMnO_3 and $\text{Y}_{1+x}\text{MnO}_3$ ($x < 0$) with varying conditions	31
4.3 Structural analysis of the asymmetric membrane.....	32

4.3.1 Structure and composition of porous support of $\text{YMn}_{0.85}\text{Ti}_{0.15}\text{O}_3$ prepared by solid state synthesis	32
4.3.2 Structure and composition of nanocrystalline $\text{YMn}_{0.85}\text{Ti}_{0.15}\text{O}_3$ prepared by citric acid method.	35
4.4 Microstructure of porous support and active layer of the membrane	37
5. Discussion	41
5.1 The influence of yttrium deficiency in YMnO_3	41
5.1.1 Structure and solubility limit	41
5.1.2 Distortion of the unit cell with varying partial pressure of oxygen	42
5.1.3 Oxygen storage ability.....	45
5.2.4 The positions of interstitial oxygen in $\text{YMnO}_{3+\delta}$	48
5.2 Structure and evaluation of the asymmetric membrane $\text{YMn}_{0.85}\text{Ti}_{0.15}\text{O}_3$	50
5.2.1 Decreased c/a ratio with titanium substitution in YMnO_3	50
5.2.2 Oxygen non-stoichiometry with titanium substitution in YMnO_3	52
5.2.3 Evaluation of the active layer and the porous supports after sintering.....	53
5.5 Further work	53
7. Conclusion.....	55
Bibliography	57
Appendix A: Structural parameters with titanium substitution in YMnO_3 within space group $P6_3cm$	I
Appendix B: Preparation of Y^{3+} and Mn^{3+} precursors for the citric acid method and gravimetrically determination of the precursors molality.....	III
Appendix C: X-ray diffraction pattern of pure phase YMnO_3 and porous support P1 made from solid state synthesis.....	V
Appendix D: Rietveld refinement of YMnO_3 and $\text{YMn}_{0.85}\text{Ti}_{0.15}\text{O}_3$ (porous support P2) prepared by solid state synthesis, and nanocrystalline $\text{YMn}_{0.85}\text{Ti}_{0.15}\text{O}_3$ made by citric acid method.	VII
Appendix E: X-ray diffractograms of yttrium deficient YMnO_3 samples annealed in N_2 and O_2 atmospheres	IX
Appendix F: Temperature program of the thermogravimetric analysis of YMnO_3 and $\text{Y}_{0.80}\text{MnO}_3$	XI

1. Introduction

Oil is the most valuable commodity in world trade today. Currently, almost 1000 barrels oil a second are used every day, but the proven reserves for fossil fuels are progressively decreasing[1]. The continuing use of fossil fuels produces harmful effects such as pollution and greenhouse gases that threatens the human health and give global warming. The steadily increasing energy needs in nowadays society forces continuous research for alternative environmentally friendly energy production techniques. One approach to meet these global demands is the continuously research on more environmentally production of syn-gas to the reforming of natural gas to liquid fuels. Both the common Fisher-Tropsch- and Methanol synthesis for reforming natural gas requires synthesis gas ($H_2 + CO$) as feedstock [2, 3]. The modern approach for production of syn-gas is the slightly exothermic partial oxidation of methane [4]. In the following schemes (1.1) and (1.2), both steam reforming and partial oxidation are illustrated.



The partial oxidation of methane requires 100 % pure oxygen to improve its performance due to the absence of nitrogen. Conventionally, oxygen separation to produce pure oxygen is a big business with nearly 100 million tons of oxygen produced every year [5]. The currently most established technique for large- scale oxygen separation is carried out by the cryogenic process [6]. This process is very expensive and energy costing, due to requirements such as low temperature and elevated pressure. An alternative is to use mixed ionic and electronic conducting (MIEC) membranes in combination with a reforming catalyst. Because MIEC membranes are 100 % selective for oxygen, the syn-gas production is reduced to just one single step. MIEC materials offer to separate oxygen from air electrochemically, and in addition to the application as oxygen permeable membranes, they are important applications e.g. cathode materials for solid oxide fuel cells and oxygen sensors [2, 3, 7].

MIEC membranes are also important in carbon capture and storage (CSS) especially in cooperation with coal power plants. [8]. "Carbon capture and storage could deliver up to 55% of the mitigation effort needed for the stabilization of atmospheric CO_2 levels by 2100", Rachel Spratt, Environmental Resource Management [9]. Coal is the most abundant and dirtiest fossil fuel, and different fossil fuel power plant concepts for CSS are currently under development, such as oxy fuel power plants. In this process the fossil fuel is combusted using pure oxygen and the result is a gas steam consisting of almost 90-95 % pure CO_2 in the dried flue gas. In the combustion process, the capturing of CO_2 can be done more easily compared than when air is

Chapter 1: Introduction

used, and stored in a safe geological site. Energy penalties can be reduced by 35 % or more by integrating dense ceramic membranes in coal power stations [6].

1.1 MIEC membranes

The two main types of oxygen separation systems based on dense ceramic membranes are (i) pure oxygen conducting membranes and (ii) mixed ionic-electronic conducting membranes (MIEC) [10]. The main difference between the two types of membranes is the driving mechanism. When oxygen diffuse through the membrane, an opposite but simultaneous flux of electrons have to charge compensate for the oxygen flux. In pure conducting materials, these electrons have to go in an external circuit, and the oxygen yield can be found from the applied current. In MIEC membranes, a gradient in oxygen partial pressure (Δp_{O_2}) is the driving force for oxygen permeation. Figure 1.1, gives a steady state profile of the chemical potential gradient across a thin MIEC membrane on a porous substrate.

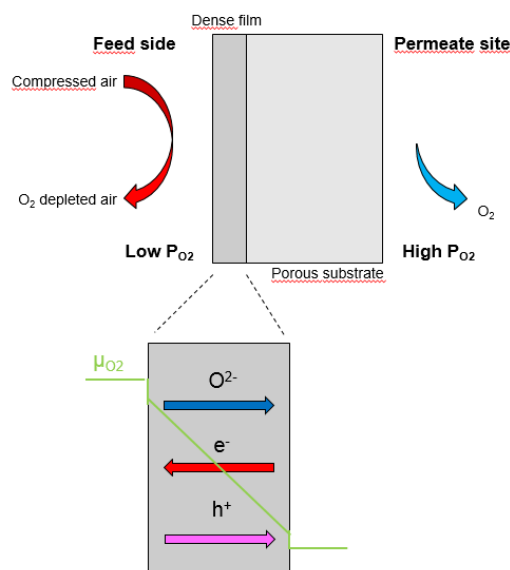


Fig 1.1: A schematic model of an asymmetric mixed ionic and electronic conducting membrane (MIEC).

Oxygen permeation through a dense MIEC membrane involves three different steps: (i) oxygen adsorption and dissociation into oxide ions, at the high partial pressure of oxygen side of the membrane, (ii) the simultaneous bulk diffusion of holes/electrons and charged oxygen (iii) release of oxide ions into molecular oxygen. The slowest moving specie or slowest process is expected to limit the rate of oxygen permeation. When the flux is governed by bulk diffusion it can generally be described with classic Wagner theory [3, 10, 11]

$$J_{O_2} = -\frac{RT}{4^2 F^2} \times \frac{\sigma_{ion}\sigma_{el}}{\sigma_{ion}+\sigma_{el}} \times \nabla\mu_{O_2} \quad (1.3)$$

Where J_{O_2} is the oxygen permeation flux in $\text{mol m}^{-2} \text{s}^{-1}$, R is the gas constant, F is the Faraday constant and σ_{ion} and σ_{el} represents the partial conductivities of oxygen ionic and electronic defects. L represents the membrane thickness and $\nabla\mu_{O_2}$ is the oxygen chemical potential gradient. Moreover, a substitution of the chemical potential with oxygen partial pressure (p_{O_2}), and an integration over the membrane thickness L between oxygen partial pressure on the air side (P_1) and on the fuel side (P_2) gives the integrated Wagner equation for bulk diffusion[2],

$$J_{O_2} = -\frac{RT}{4^2 F^2 L} \times \frac{\sigma_{ion}\sigma_{el}}{\sigma_{ion}+\sigma_{el}} \times (\ln P_1 - \ln P_2) \quad (1.4)$$

Consequently, reducing membrane thickness for bulk controlled diffusion will increase the O_2 permeation rate [12]. For thinner membranes, the resistance to oxygen ion conduction will be decreased until a certain limit, known as the critical thickness (L_c), which also depends on operating conditions. There are few reports concerning thin films of hexagonal $YMnO_3$, while for the perovskite structure, a critical film thickness should be $25 \mu\text{m}$ or less[12]. For thin membranes, a porous support is needed for mechanical stability also referred to as an asymmetric membrane. For a thickness below L_c , the interphase of the membrane becomes the region of higher resistance, shown in Figure 1.2a. Wagner equation is not applicable when the oxygen becomes determined by the surface exchange reactions. Decreasing partial pressure of oxygen (P_{O_2}) gives increased control of oxygen flux by surface kinetics, Figure 2.1b.

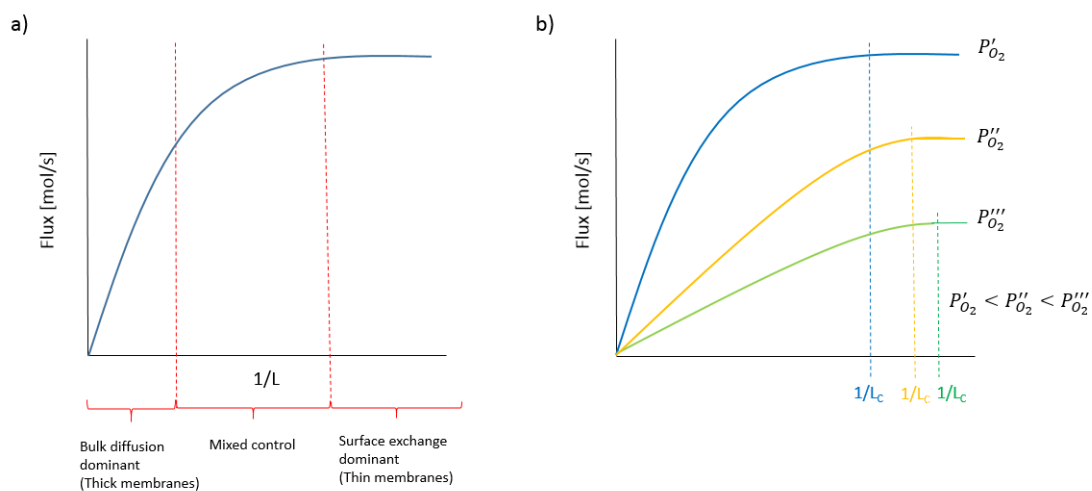


Fig. 1.2: Oxygen flux through membrane as a function of the reciprocal thickness of the membrane $1/L$. a) As the membrane becomes thinner, the oxygen flux is increasingly dominated by surface exchange kinetics, b) Decreasing P_{O_2} leads to increased control of oxygen transport by surface kinetics. $1/L_c$ is the reciprocal characteristic thickness where surface exchange is dominating.

Chapter 1: Introduction

The critical thickness can be expressed by the surface exchange coefficient (k_{chem}) and the chemical diffusion coefficient (D_{chem}) as follows [2, 13],

$$L_C = \frac{D_{chem}}{k_{chem}} \quad (1.5)$$

For asymmetric membranes with a thickness value less than L_C , the surface exchange coefficient k_{chem} is the limiting factor for oxygen permeation. Thus no further increase in oxygen flux is feasible without increasing k_{chem} .

1.1.1 Material requirements

A major challenge in processing supporting MIEC membranes is the selection of a suitable fabrication method and materials for the porous substrate, taking into account requirements as chemical compatibility, similar thermal expansion coefficient, good mechanical strength and porosity for adequate diffusion of gas [8, 12]. In addition, stability in reducing atmospheres, membrane design, sealing and costs are important factors in processing MIEC membranes.

Non-stoichiometric oxide materials have been heavily researched because of their reversible oxygen storage/release capacities (OSC), and the most used dense ceramic membranes today are perovskite or fluorite structures [5, 10, 14]. Several perovskite materials have demonstrated high OSC values ($>2500 \mu\text{m-O/g}$) and low re-oxygenation temperatures ($< 200 \text{ }^\circ\text{C}$) [14]. However, these materials require either a reducing atmosphere or high temperatures ($> 700 \text{ }^\circ\text{C}$) to form oxygen vacancies. The challenge for MIEC membranes today are the long-term chemical and mechanical stability associated with the high operating temperatures. The chemical driving force for oxygen permeation can cause chemical degradation in the material, and further on, a difference in mobility of the cations in the structure can lead to decomposition [15]. A lot of research is focusing on trying to increase the oxygen flux and to reduce the operating temperatures for the MIEC materials to below $700 \text{ }^\circ\text{C}$, since lower operating temperatures reduce energy consumption and thermal degradation of the membrane [10]. A very recent work from Remsen et al. [14] showed that hexagonal $\text{DyMnO}_{3+\delta}$ can accommodate a large excess of oxygen up to $\delta=0.35$. In Figure 1.3, the reversible absorption of large amounts of oxygen around $200\text{-}300 \text{ }^\circ\text{C}$ and sharply desorbed oxygen at elevated temperatures is shown for $\text{DyMnO}_{3+\delta}$. Hence, it is suggested that hexagonal manganites have the ability to accommodate oxygen interstitials and thus have ionic conduction at lower temperatures. This is promising for the next generation of MIEC membranes because it may solve the problems with long-term stability due to the high operating temperature used today.

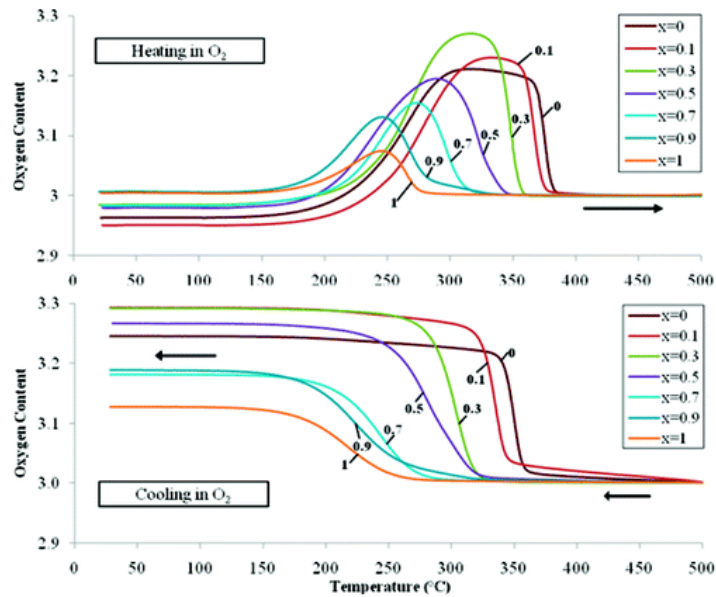


Fig. 1.3: Oxygen content as a function of temperature for $\text{Dy}_{1-x}\text{Y}_x\text{MnO}_{3+\delta}$ with a heating/cooling rate of $0.1\text{ }^\circ\text{C/h}$. Figure is reprinted from Remsen et.al [14].

As the name “MIEC membrane” states, both ionic and electronic conductivity are important material requirements. Ionic conductivity often relates to defects in the crystal structure, while electronic conductivity often is associated with electronic defects [10]. A defect is an imperfection in the crystal structure that differentiate a perfect crystal (only at 0 K) from a crystal. The concentration of defects in crystalline solids are important because they can modify important properties [16].

The perovskite structure of LaMnO_3 is known to have a degree of freedom in cation stoichiometry [17]. It is therefore natural to investigate the same phenomenon in hexagonal manganites. YMnO_3 is one of the most studied hexagonal manganite [18], and due to the layered structure of hexagonal manganites, an decrease in yttrium content will be interesting. Since yttrium oxide is an expensive oxide, it will be beneficial to investigate the ability of decreasing the yttrium content in the structure.

1.2 Research objectives

This thesis has two primary goals, the first one will be to examine how yttrium deficiency impacts the hexagonal structure of YMnO_3 . It will be investigated how the lattice parameters change from yttrium deficient samples prepared in air atmosphere in addition to be annealed in O_2 and N_2 rich atmospheres. This is to get a better understanding of the defect chemistry in YMnO_3 , since hexagonal manganites have the possibility to accommodate interstitial oxygen. The second goal is to investigate the possibility of using hexagonal $\text{YMn}_{0.85}\text{Ti}_{0.15}\text{O}_3$ as an oxygen permeable membrane. Titanium substitution was chosen due to its ability to reduce microcracking in YMnO_3 , as titanium has proven to reduce the anisotropic thermal expansion and porosity in YMnO_3 . However, the origin of microcracking will not be investigated in this

Chapter 1: Introduction

thesis. The aim is to fabricate an asymmetric membrane consisting of an active layer on top of a porous support. The same composition will be used for both the active layer and the support to avoid capability problems, which can lead to degradation or cracking. It is important to understand the conditions necessary for a successful preparation of the membrane, as it has never been done before for hexagonal YMnO_3 . Known synthesis methods for YMnO_3 are going to be used in addition to a successful technique used in production of perovskite asymmetric membranes.

2. Literature survey on YMnO₃

Rear-earth manganites with their competing orthorhombic and hexagonal crystal structures, with 6- and 5 folded coordinated Mn³⁺, have been studied for over 50 years [14]. The hexagonal manganites has attracted much interest, especially in recent times, because of the coexistence of ferroelectricity and antiferromagnetic order [19]. However, most multiferroic manganites are insensitive to applied magnetic fields due to their antiferromagnetic order. This is a disadvantage in potential applications.

Among hexagonal manganites, YMnO₃ is the most studied metal oxide[20]. Bulk YMnO₃ has a high ferroelectric transition temperature $T_c \sim 913\text{K}$ [21] and a low antiferromagnetic transition temperature $T_N \sim 70\text{-}80\text{K}$ [22, 23]. One can note that literature shows a large spread of T_N . Increased attention should be given to off-stoichiometry effects for the understanding of the physical properties of hexagonal YMnO₃. Unlike perovskite thin films, YMnO₃ does not possess a critical film thickness and is therefore a promising candidate for making multiferroic devices in nano scale. Thin films of YMnO₃ have also potential in non-volatile ferroelectric random access memory devices.

2.1 Crystal structure

The isostructural RMnO₃, where R is a transition or a rare earth metal, can crystallize in either hexagonal or orthorhombic structures. Large rare-earth elements like Dy, Tb and Gd prefers the orthorhombic structure with room temperature space group *Pbnm* [17]. For smaller ions like Y, Sc, Ho-Lu and In, the hexagonal structure with space group *P6₃cm* (No. 185) is the preferred ground-state structure.

Hexagonal YMnO₃ with space group *P6₃cm* consist of Mn³⁺ ions coordinated by two apical and three planar oxygen atoms with corner sharing atoms in the *ab*-plane. This forms a trigonal bipyramidal environment around the Mn ions. Each consecutive layer of MnO₅ is rotated along the *c*-axis by 180 ° [10, 11]. The bipyramids are tilted with respect to the *ab*-plane by $\sim 8^\circ$ and to the polar *c*-axis by $\sim 5^\circ$ [17]. Situated between the MnO₅ layers lies Y³⁺ coordinated by 7 oxygen ions. The displacement of Y atoms along the *c*-axis for the low temperature phase are 2/3 in negative direction and 1/3 in the positive direction[14]. The small displacement of the trigonal bipyramids compared to the Y³⁺ layer gives rise to a spontaneous polarization of $\sim 5\text{-}6\mu\text{m}/\text{cm}^2$ [24]. The main driving force for polarization is electrostatics although partial covalency is found between empty Y 4d orbitals and O 2p orbitals[24, 25]. Hexagonal YMnO₃ are therefore referred to as a “geometric ferroelectrics”.

Above the transition temperature (trimerisation temperature), YMnO₃ exhibits a paraelectric structure with space group *P6₃/mmc* (No. 194) [11]. This is a less ordered structure with higher symmetry than the low temperature phase. In this phase compared to the polar *P6₃cm* are the MnO₅ bipyramids not tilted and the Y³⁺ ions are not displaced. The unit cell of the two different space groups are shown in Figure 2.1, and the space group *P6₃/mmc* is presented with a *P6₃cm*

basis to allow comparison. Green atoms displays Y^{3+} , red atoms O^{2-} and purple polyhedra show the trigonal bipyramids MnO_5 .

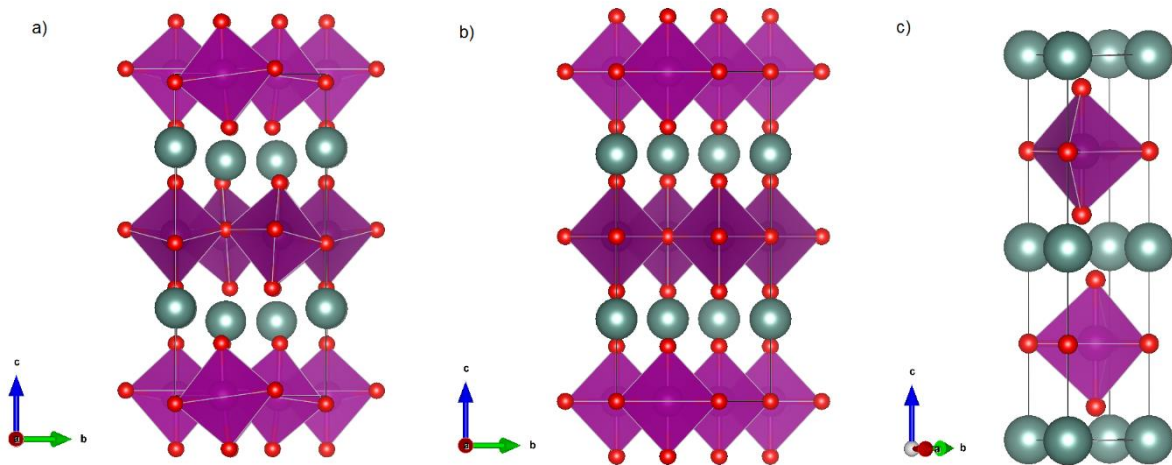


Fig. 2.1: a) The low temperature space group $P6_3cm$. b) The high temperature phase with space group $P6_3cm$ basis c) The high temperature phase $P6_3/mmc$. Green atoms displays Y^{3+} , red atoms displays O^{2-} , the purple trigonal bipyramids indicates MnO_5 with black Mn^{3+} in the middle. Figure is drawn using VESTA software[26] and atomic positions are from Gibbs et al. [27]

The manganese ions in space group $P6_3cm$ are displaced both in the basal plane and in the c -direction. The difference in bond length between Mn-O in-plane and out-of-plane is reported to be 2.05 Å and 1.86 Å respectively [28]. Onset of the bipyramidal tilting at the trimerisation temperature triples the unit cell volume from space group $P6_3/mmc$ to $P6_3cm$ and is given by the following [4]:

$$3^{\frac{1}{2}}a(P6_3/mmc) = a(P6_3cm) \quad (2.1)$$

The temperature of onset for trimerisation of MnO_5 and polar displacement of Y^{3+} , as well as the driving force for polarization have been discussed in several reports. Since the phase transition between the two polymorphs is a second order phase transition, it has been argued from group theory and high temperature x-ray diffraction (HTXRD) that hexagonal manganites must undergo two structural transitions, and that there exist an intermediate phase with space group $P6_3/mcm$ [24, 29]. Recent experiments does not support the notation of an intermediate phase. The ferroelectric to paraelectric phase transition have been reported to be around 1250 K [27], but some structural anomalies have been reported around the Curie temperature, but this is not well understood[24, 29]. Selbach et.al[24] found a direct and continuously transition from $P6_3cm$ to $P6_3/mmc$ obtained by HTXRD in both N_2 and air atmosphere, with no indication of intermediate phase. In a study performed by Bergum et.al [17], a second order transition in YMnO_3 at 1020 °C was found by HTXRD in oxygen atmosphere and by dilatometry. There were no indications of contraction or expansion of YMnO_3 between N_2 and O_2 atmospheres.

2.2 Phase stability

The orthorhombic and hexagonal polymorphs are close in energy. The binary oxides forming YMnO₃ is given by the following:



Since reactions, involving only solids expects to have an entropy close to zero, the enthalpy of the reaction dominates the Gibbs energy. Yokokawa et.al [30] were the first to report the empirical relationship between the Goldschmidt's tolerance factor t and the enthalpy of formation of perovskite from their constituent binary oxides. This relationship has also been shown to be valid for manganites[17], and thus the relative stability between the hexagonal and the orthorhombic structures depends on the Goldschmidt's tolerance factor [31],

$$t = \frac{r_a + r_o}{\sqrt{2}(r_b + r_o)} \quad (2.3)$$

As seen from (2.3), the tolerance factor is dependent on the radius of each component in an ABO₃ structure. The hexagonal phase is stable for a tolerance factor of $t < 0.855$, while the perovskite phase is stabilized for a tolerance factor in the range $0.855 \leq t \leq 1$ (Calculated using Shannon's values at room temperature[32]) [33]. The calculated Goldschmidt's tolerance factor for YMnO₃ is 0.854, which is close to the geometric stability limit of the perovskite structure. The hexagonal structure is stabilized for YMnO₃ due to the small yttrium ions that wants to lie in layers instead of in between octahedral. The lower the tolerance factor, the less exothermic the enthalpy of reaction (2.2) and for hexagonal YMnO₃ it is reported to be -29.8 ± 2.1 kJmol⁻¹. This value is about 1/3 of the corresponding value for orthorhombic LaMnO₃. [17]

According to a study on the thermodynamics of the Y-Mn-O system[34] in air, seen in Figure 2.2, hexagonal YMnO₃ is metastable for temperatures less than 789 °C and entropy stabilized with respect to Y₂O₃ and YMn₂O₅ above this temperature. However, the hexagonal structure is considered stable at room temperature because the transition from orthorhombic to hexagonal phase is reconstructive, and therefore expected to be slow with a high activation energy barrier. The metastability can be extended to larger temperature intervals [24, 34]. Above 1794 °C, the hexagonal phase melts incongruently to α -Y₂O₃(s) and liquid.

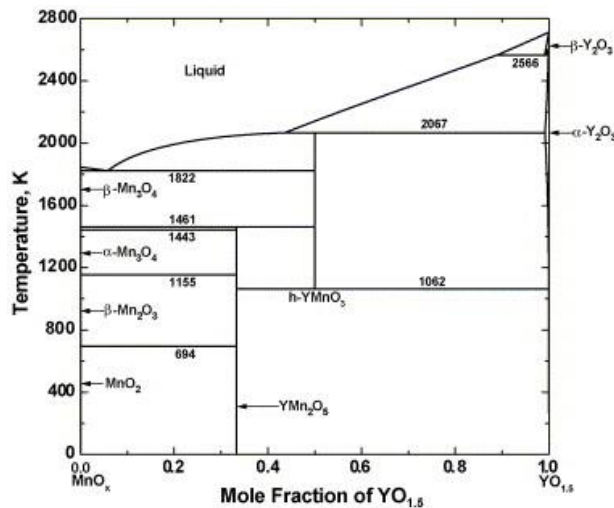


Fig. 2.2: Phase diagram for the Y-Mn-O system. Figure is reprinted from Chen et.al [34]

The metastable and denser orthorhombic perovskite forms easily at high pressures or through epitaxial stabilization. Oxidizing conditions and low temperature chemical synthesis routes also favour the perovskite structure. Oppositely can the hexagonal phase be stabilized with epitaxial growth, single crystal growth or by reducing conditions[24]. Since the phase formations are affected by oxidizing/reduction conditions it is suggested by Selbach et.al[24] that oxidizing/reduction of a fraction of Mn^{3+} to $\text{Mn}^{4+}/\text{Mn}^{2+}$ readily can shift the stability of the two phases. This is also suggested by Bergum et.al[17], since both the enthalpy and entropy of reaction (2.2) can be argued to be small. A possible oxidation of Mn^{3+} to Mn^{4+} may have a large effect of the polymorph stability since there exists a substantial enthalpy involved in the oxidation of Mn^{3+} to Mn^{4+} . As Mn^{4+} is smaller than Mn^{3+} , the oxidation of a fraction of Mn^{3+} will increase the average Goldschmidt's tolerance factor of the system. The Shannon radius for the high spin cations Mn^{3+} and Mn^{4+} are 0.645\AA and 0.53\AA respectively [32]. An illustration showing the different radii of manganese with different valence states is shown in Figure 2.3.

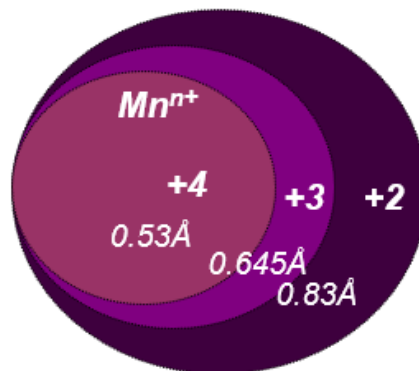


Fig 2.3: Shannon ionic radius for different valence states of Mn (HS). Values are obtained from [32]

The orthorhombic perovskite LaMnO₃ has been found to display a degree of freedom in oxygen stoichiometry in the range 2.947-3.079 at 1200 °C, while the corresponding range for hexagonal YMnO₃ was found to be 2.963-3.009[17]. As the perovskite structure can accommodate a higher degree of excess oxygen due to partial oxidation of Mn³⁺ to Mn⁴⁺, it is therefore expected that oxidizing conditions favour the formation of the orthorhombic perovskite phase. Oxidation of Mn³⁺ is known to influence the phase stability and crystal structure of the multiferroic perovskites BiFe_{1-x}Mn_xO_{3+δ} and BiMnO_{3+δ}.

2.2.1 Crystal field stabilization

A contribution to stabilize the hexagonal structure of YMnO₃ is the trigonal bipyramidal crystal field stabilization energy associated with the four electrons in the d-orbital of Mn³⁺ [35]. The trigonal bipyramidal and octahedral crystal field splitting for hence hexagonal and orthorhombic phases is represented in Figure 2.4. The red circles in the figure represents the d⁴ electron of Mn³⁺.

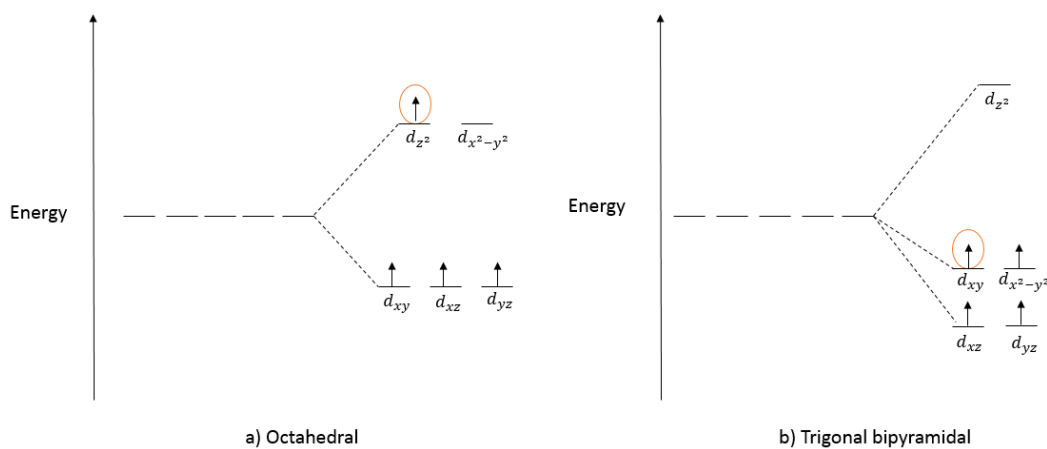


Fig. 2.4: a) Octahedral crystal field splitting, b) trigonal bipyramidal crystal field splitting. Marked arrows represents the d⁴ electron of Mn³⁺.

The lowest excitation limit for a d⁴ electron in the trigonal bipyramidal crystal field splitting is up to the fairly localized z² orbital. This energy difference depends sensitively on the Mn-O distance within space group *P6₃cm* [28].

2.3 Thermal and chemical expansion of the structure in varying atmospheres

The lattice parameters *a* and *c* of hexagonal YMnO₃ experiences anisotropic chemical and thermal expansion upon heating [24, 27, 36]. Thermal expansion is a linear trend, and is a

volume change that the material experience upon a temperature change. The additional expansion, when there does not exist a linear trend is called a chemical expansion. The difference between chemical and thermal expansion can be seen in Figure 2.5.

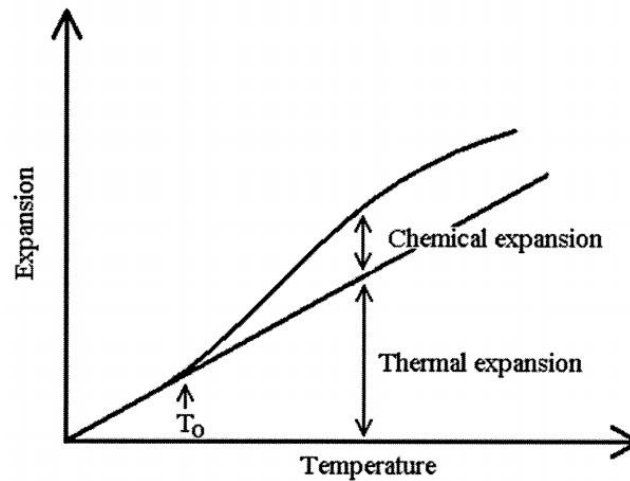


Fig. 2.5: The contribution of chemical expansion to the thermal expansion. The onset of thermal reduction is T_0 . Figure is reprinted from H.Lein[12]

Selbach et.al [24] found the anisotropic relationship in air, nitrogen and oxygen atmosphere for hexagonal YMnO_3 and HoMnO_3 and is seen in Figure 2.6. The lattice parameter c for HoMnO_3 decreases non-linearly to the trimerisation temperature (T_s) around 1300 K, where it has close to zero thermal expansion for about 100 K before it increases with temperature. The increase in unit cell parameter c is more rapid above T_s in N_2 compared to air atmosphere. The same behavior is observed for YMnO_3 , but it is not seen in Figure 2.5 as the data is collected in the temperature range below 1400 K. However, the unit cell parameter a is smaller in air compared to N_2 atmosphere, and the difference increases with increasing temperature. The changes in slopes at temperatures 1200 K and 1300 K for the lattice parameter a in HoMnO_3 , have also been reported by Nenert et al[37] for YMnO_3 .

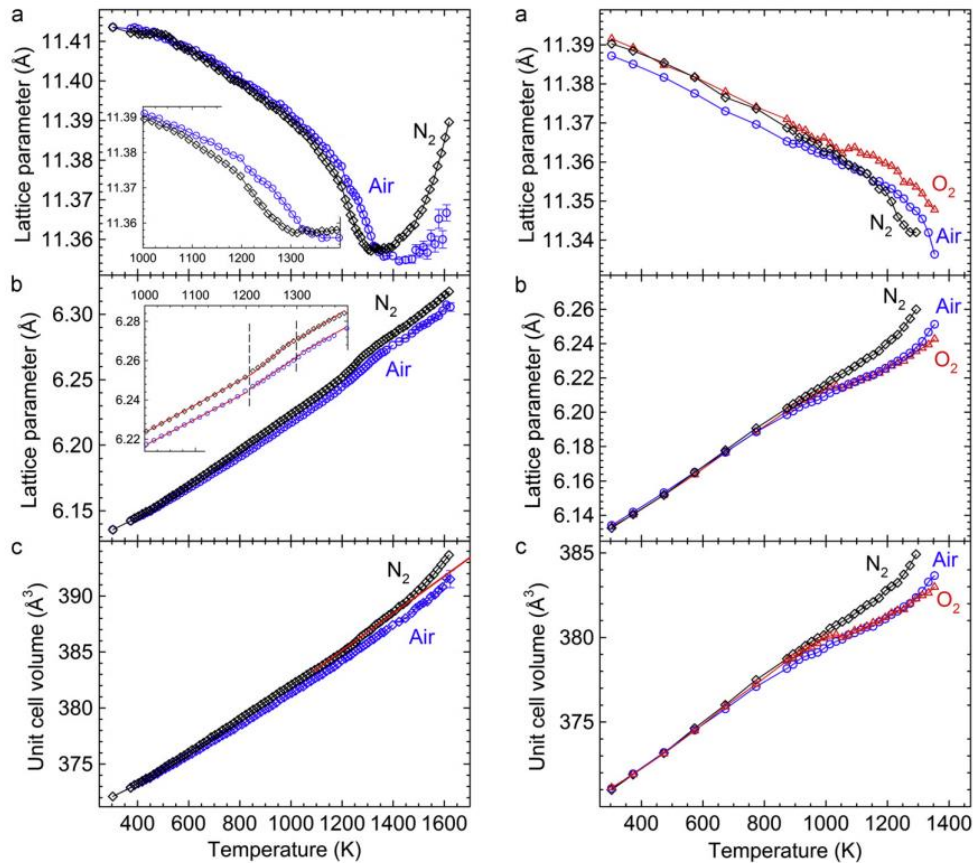


Fig. 2.6: a) Changes in unit cell parameter c , (b) lattice parameter a and (c) unit cell volume for hexagonal YMnO_3 HoMnO_3 in O_2 , N_2 and air atmosphere. Figure is reprinted from Selbach et.al[24].

The increase of the unit cell parameter a with temperature, is assigned to thermal expansion in the material, while the decrease in unit cell parameter c is related to ferroelectric distortion as the alignment of MnO_5 bipyramids causes Y^{3+} to contract[15]. From about 650 K, the unit cell volume is larger for N_2 than air. The anisotropic chemical expansion for both YMnO_3 and HoMnO_3 is an indication that the oxygen content is sensitive to partial pressure of oxygen. The symmetry and cell dimensions in hexagonal YMnO_3 depends on oxygen content in the structure and its effect on the crystal structure has received little attention. The chemical expansion seen at higher temperatures is attributed to oxygen vacancies in the material.

2.3.1 Microcracking as a result of anisotropic expansion

Application of polycrystalline YMnO_3 is limited by porosity and grain boundary microcracking, which affects the mechanical and physical properties of the material. Tomczyk et.al [36] were the first to address the microcracking observed in YMnO_3 . A volume change of 3.7 %, which generated an internal stress of 200 MPa, and a high anisotropic thermal expansion coefficient in the temperature range 600-1000 was found to be the origin of microcracking. The high temperature phase transition from $P6_3/mmc$ to $P6_3cm$ which is reflected through the differences in a and c lattice parameters during heating, is associated with the high volume change. It is known that phase transitions that involves ionic rearrangement often is associated with a volume change. In addition can thermal expansion in highly crystalline structures give

Chapter 2: Literature survey on YMnO_3

spontaneous microcracking upon cooling[38]. Besides decreasing the grain size below a critical value, suitable doping can give a reduction of both the volumetric change and the anisotropic thermal expansion. Ti substitution, recently shown by Tomczyk et.al[36], have an effective way to reduce the microcracking in YMnO_3 .

2.3.2 Substitution with titanium in YMnO_3

As mention above, increased concentration of Ti in YMnO_3 , decreases the concentration of microcracks and intergranular porosity[39]. This is because increased Ti substitution has shown to increase the unit cell parameter a , and decrease the unit cell parameter c , up to $x=0.15$ [15, 39]. This gives a decreased c/a – ratio for the hexagonal unit cell which in turn reduces the anisotropic thermal expansion in the high temperature phase transition from $P6_3/mmc$ to $P6_3cm$. With X-ray diffraction this phase transition can be seen especially by the disappearance of the reflections at 23° and $36^\circ 2\theta$ for $x=0.15$. The experimental unit cell parameters for Ti substitution in YMnO_3 for $x = 0.05, 0.10$ and 0.15 refined within space group $P6_3cm$ was found by S.Nesdal [15] and are found in Appendix A. Increased titanium substitution (up to $x=0.15$) in YMnO_3 have also in recent preliminary master's thesis [40] shown a high conductivity compared pure YMnO_3 . At 400°C , the conductivity of $\text{YMn}_{0.85}\text{Ti}_{0.15}\text{O}_3$ was $2 \cdot 10^{-3} \text{ S/cm}$ compared to ranges of 10^{-6} S/cm for YMnO_3 . For increased Ti content above $x=0.175$, a rhombohedral phase with space group $R3c$ or $R3c(\text{bar})$ is observed by Asaka et.al[41].

2.4 Oxygen non-stoichiometry and defect chemistry of YMnO_3

2.4.1 Point defects

The simplest defect imaginable in a crystal is an imperfection at a single atom site. These defects are called point defects and can be divided into intrinsic and extrinsic point defects. Intrinsic point defects involve addition or removal of an atom in the structure, while the extrinsic point defects are defects that result by doping with an impurity atom. The two types of point defects that can occur in a pure material are; (i) vacant atom sites, or vacancies, or (ii) interstitial atoms occupying lattice sites which are normally not occupied in the crystal. A representation of an interstitial atom and a vacancy is seen in Figure 2.7.

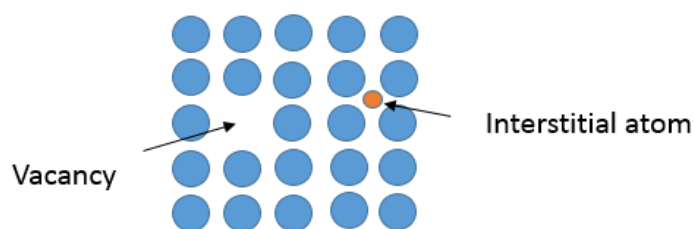


Fig. 2.7: Point defects in a perfect periodic structure.

Such vacancies and interstitials are always present even in the purest material. For these defects to be stable, the free Gibbs energy (ΔG) of a crystal containing defects must be less than the free Gibbs energy of a crystal not containing defects[16].

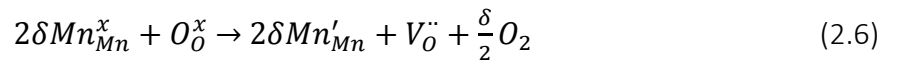
$$\Delta G_{\text{crystal with defects}} < \Delta G_{\text{pure crystal}} \quad (2.4)$$

The concentration of defects will be in a thermodynamic equilibrium at a given temperature. This equilibrium concentration corresponds to the minimum in Gibbs free energy, which is dependent on the enthalpy of defect formation (ΔH) and entropy of configuration (ΔS). Defects can be induced by exposing the material for a certain environment, for example a low partial pressure of oxygen to favor oxygen vacancies or oxygen rich atmosphere to induce interstitial oxygen.

The presence of oxygen vacancies in hexagonal YMnO₃ is controversial. It has been reported that oxygen vacancy defects exists [42], whereas the presence of oxygen vacancies within hexagonal YMnO₃ was claimed unlikely [37]. Cation diffusion is anyway not pronounced in hexagonal manganites up to a temperature of 1000K, which suggests creation of interstitial oxygen at lower temperatures without formation of oxygen vacancies. The hexagonal phase of YMnO₃ is also less dense compared to the known orthorhombic structure, which may give more sites for interstitial oxygen in the structure. Overton.et.al[43] suggests that oxygen vacancies will preferably leave planar site in the MnO₅ bipyramids. A chemical expansion for both unit cell parameters a and c was found with decreasing oxygen in the structure of YMnO₃. The defect reaction for an oxygen vacancy in YMnO_{3- δ} is given by the following:



Written in Kröger-Vink notation this becomes



It is suggested that one oxygen vacancy will affect two Mn atoms. The charge compensated electrons are assumed to be localized on Mn because Mn has several possible oxidation states. The oxidation state for Mn will be reduced from 3+ to 2+ and Mn change from 3d⁴ to 3d⁵.

Chapter 2: Literature survey on YMnO₃

With the same explanation as for oxygen vacancies, it is suggested for interstitial oxygen in YMnO_{3+δ} that the charge compensated holes are localized around Mn. The oxidation state of the two Mn atoms will be oxidized from 3+ to 4+ and Mn change from 3d⁴ to 3d³. The defect reaction of interstitial oxygen in YMnO_{3+δ} is given by the following:



In Kröger-Vink notation this becomes



2.4.2 Electronic defects

The electronic defects in a material are associated with excitation of electrons from valence band (VB) to the conduction band (CB), intrinsic ionization or formation to keep charge balance in the material [10]. In non-stoichiometric oxides, the concentration of electronic defects usually relates with oxygen excess or oxygen deficiency. Thus for perovskites, metal excess or oxygen vacancies are accompanied by formation of electrons, which acts as the major charge carriers in the material and is responsible for the n-type electronic conductivity. In the opposite manner, metal deficiency or oxygen interstitial creates electron holes, which results in a p-type semiconductor, where the electronic conductivity occurs by transport of electron holes in the valence band. To achieve higher conductivity, doping with an aliovalent cation can cause oxygen excess or oxygen deficiency.

YMnO₃ is a poor p-type semiconducting material[44] with a believed mechanism for conduction found to be thermally activated hopping of small polarons between Mn³⁺ and Mn⁴⁺, and migration of oxygen vacancies at higher temperatures [45]. The overlap of Mn orbitals in the basal plane is therefore suggested to be the conductive state for hexagonal manganites [24]. A polaron is a quasiparticle used to describe the interaction between an electron and atom in solid materials[46]. This quasiparticle can be described as an electron with a polarization cloud. As the electron moves around, it will drag the polarization cloud with it, which results in a higher inertial mass and lower mobility compared to a free electron.

The Nernst-Einstein equation are used to relate the activation energy of polaron hopping and the temperature dependence of the mobility for an electron or hole

$$\mu = Ae^{-\frac{E_a}{RT}} \quad (2.11)$$

Where E_a is the activation energy for polaron hopping, R is the gas constant, A is a pre exponential factor and T is the absolute temperature. The latter relation also holds for ionic conductivity, because the process of polaron hopping is similar to ion hopping between neighbouring sites. Thus, the mobility of an ion increase with increasing temperature. In many cases, the electronic conduction dominates the total conductivity in a material, because the mobility of electrons is about 1000 times higher compared to the mobility of ions in the lattice [15].

2.5 Theory on synthesis methods

2.5.1 Sol gel synthesis

Synthesis of nanocrystalline hexagonal YMnO₃ used in this project was adapted from Bergum et al[17], which is a modified Pechini method. This method has successfully synthesized nano-sized crystalline powder of YMnO₃. Nitric acid was avoided due to increased stabilization of the metastable orthorhombic phase. Ethylene glycol in equal amounts to the citric acid has shown to have a significant effect on suspending the cations in the solution in addition to helped polymerize and to avoid precipitation. There was shown to be a clear trend in increasing crystallite size with increasing annealing temperature and above approximately 750° C, the crystallite size was dependent on kinetics. An annealing temperature of 825 °C of the raw powder gave a crystallite size of 32 nm, while at 900 °C a crystallite size of 52 nm was obtained.

2.5.2 Solid state synthesis

Solid state synthesis is a widely used method for preparation of bulk YMnO₃. This synthesis involves mixing binary oxides with a mortar and pestle followed up by heating treatment (firing). It is important that the particles are homogeneously mixed in the mortar, and that the particle size is small and uniform. To ensure that the reaction by diffusion occurs at the particle interphase during heating, the powder is pressed into greenbodies, which leads to smaller diffusion distance between the particles. For binary oxides with high coordination numbers, a lot of energy is needed to overcome the energy barrier in the lattice and diffuse over to another site. For such oxides, high temperature is needed. The reaction rate also depends on temperature and by increasing the temperature, the reaction rate increases. The rule of thumb is to use temperatures that are 2/3 of the materials melting temperature. For YMnO₃, one firing at temperature 1350 °C is often not enough to obtain a pure hexagonal phase[47]. Regrinding, pressing and reheating is necessary to ensure reorientation of the powder to bring more particle surfaces in contact. Different atmospheres during heating can be used to adjust the ion oxidation state in YMnO₃. Reducing atmosphere (N₂) adjusts the low valence state, while oxidizing atmosphere (pure O₂) ensure high valence state[15]

Chapter 2: Literature survey on YMnO_3

2.5.3 Solid state sintering

Since most of the samples prepared in this master thesis are polycrystalline ceramics, they need to be solid state sintered. The term “sintering” refers to the pore shrinkage, pore shape change, and grain growth which particles in contact undergo during heat treatment[48]. The major driving force of the sintering process is the achievement of minimum free energy in the material. The possible mass transport mechanisms for solid state sintering are given in Fig 2.5 [49]. The driving force for evaporation-condensation is the difference in vapour pressure for convex and concave surfaces. While for surface diffusion, lattice diffusion from surface, lattice diffusion from grain boundaries and grain boundary diffusion the driving mechanism is vacancy concentration across curved surfaces. Since these mechanisms depend on the activation of material transport, they are strongly temperature dependent. Higher sintering temperatures are needed when the material exhibits stronger bonds in the crystal lattice. Polycrystalline samples of YMnO_3 need high sintering temperature, and densities of >90 % have been reported when sintered at 1450 °C for 10 hours [24].

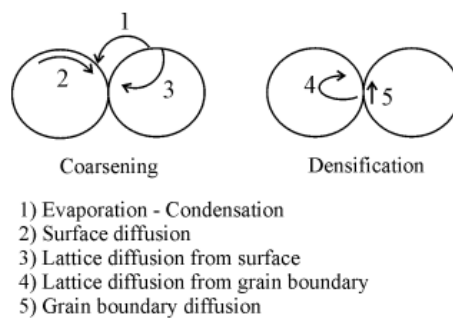


Fig 2.8: Mass transport mechanisms in solid state sintering.

During the first stage of the sintering process, a very small degree (~5 %) of densification occurs, but neck formation between particles are occurring by surface diffusion (and evaporation-condensation if the vapor pressure is high enough). In this stage, the pores are open with interconnected porosity. Most of the densification (~94 %) occurs in the intermediate stage and grain boundaries are created. The pores are still open, but smaller compared to the first stage. At the end of the intermediate stage, the grain growth starts. During the final stage of the sintering process, the last part of densification occurs. The pores are closed, and are so small that they cannot hinder grain growth. Large agglomerates in the powder is important, as these will act as large particles that might be responsible for exaggerated grain growth.

3. Experimental

In this chapter, the experimental methods used for this project is described. A list of the used binary oxides and other chemicals, their purity and manufacturers are listed in Table 3.1.

Tab. 3.1: List of used binary oxide, manufactory and purity.

Binary Oxides	Molecular formula	Purity	Manufactory
Yttrium(III) oxide	Y_2O_3	99.99 wt-%	Sigma-Aldrich
Manganese(III) oxide	Mn_2O_3	99.0 wt-%	J.T Baker
Titanium(IV) oxide	TiO_2 (anatase)	99.80 wt-%	Sigma-Aldrich
Activated charcoal	C	≥ 98 wt- %	Merck KGaA
Ethylene glycol	$C_4H_6O_6$	99 %	Merck
Manganese(II)carbonate hydrate	$Mn(CO_3) \times H_2O$	99.5 wt-%	Sigma-Aldrich
Yttrium(III) acetate hydrate	$Y(O_2C_2H_3)_3 \times H_2O$	99.9 wt-%	Sigma-Aldrich
Titanium(IV) isopropoxide	$Ti(OCH(CH_3)_2)_4$	97 wt-%	Sigma-Aldrich
Citric acid	$C_6H_8O_7$	>99.0 wt-%	Merck
Reagent grade ethanol	C_2H_6O	≥ 99.8 vol-%	VWR International / Sigma Aldrich

3.1 Preparation of powders and sintered samples

3.1.1 Solid State synthesis of crystalline powder

Preparation of $YMnO_3$ and yttrium deficient $YMnO_3$ powder

All samples of $Y_{1+x}MnO_3$ for $x=-0.05$ to $x=-0.30$, including $YMnO_3$ were prepared by conventional solid state synthesis. Prior to use, the binary oxides were dried at 500 °C for 12 hours. Around 200 °C, the oxides were moved from the furnace and kept in a desiccator, where they after short time were weighed out in stoichiometric amounts. The reactants were thoroughly mixed in an agate mortar, before uniaxial pellets of 15 mm were immersed in sacrificial powder on alumina crucibles and fired once in a clean furnace in air at 1450 °C for 12 hours. The used heating and cooling rates was 200 °C/h for every samples.

Chapter 3: Experimental

Preparation of porous supports for the asymmetric membrane

The stoichiometric powder of $\text{YMn}_{0.85}\text{Ti}_{0.15}\text{O}_3$ to be used for the porous support was also synthesized by the solid state method. The binary oxides were mixed with carbon black (pore former), and fed into a 250 ml polyethylene bottle. The ratio between carbon black and the total weight of oxides was 1:5. The bottle was filled with yttrium stabilized zirconia (YTZ) grinding media (\varnothing 5mm), and to achieve a slurry, reagent grade ethanol was added until it reached $\frac{3}{4}$ of the bottle volume. Table 3.2 gives the composition of the porous powder mixture.

Tab 3.2: Composition of porous $\text{YMn}_{0.85}\text{Ti}_{0.15}\text{O}_3$ powder mixture.

Chemical	Amount [g]	Amount [wt-%]
Mix of binary oxides: Y_2O_3 , Mn_2O_3 , TiO_2	20.01	83.33
Carbon black	4.002	16.67
Total mixture	24.01	100.0

The milling time for the slurry was 16 hours, before the grinding media was removed and the slurry was dried in a rotation evaporator. The dried powder was mortared for a short time, before it was uniaxial pressed into pellets with diameters of 30mm and heights of 4-5mm. The temperature program for calcination and sintering of the pellets, seen in Figure 3.1, was chosen to eliminate the pore former and to gain some structural strength to the support. A slow heating rate and dwell step at 500°C was used to ensure slow burn-off of carbon black, which in turn reduces the probability of destroying the support. The burn-off of carbon was performed in a calcination furnace, while sintering at higher temperatures was performed in a clean furnace. The density of the substrates were measured after sintering by a caliper, followed by a characterization in XRD. The first pellet that was made (P1) was first sintered at 1200 °C for 1 hour in air after the carbon burn-off. This gave a non-phase pure sample, and a second firing at same temperature and time was done in N_2 atmosphere. The second pellet (P2) was only sintered in N_2 atmosphere, as seen in Figure 3.1.

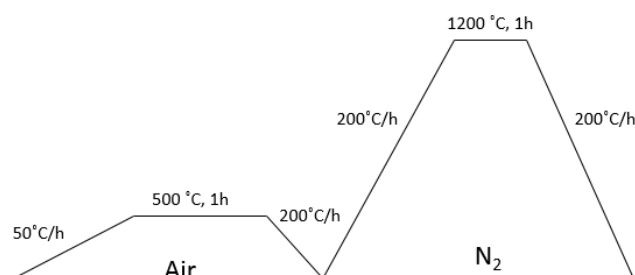


Fig 3.1: Temperature program used during sintering of porous support ($\text{YMn}_{0.85}\text{Ti}_{0.15}\text{O}_3$).

3.1.2 Preparation of the active layer – citric acid method

The citric acid synthesis method described in this section is based on Bergum et.al[17], who published a paper given a synthesis route yielding nanocrystalline YMnO_3 . Nanocrystalline powders was made to ensure that the dip coating results in a homogeneous layer on top of the porous support.

Nanocrystalline powder was prepared by stoichiometric amounts of Y^{3+} - and Mn^{3+} precursors and the Ti^{4+} precursor titanium isopropoxide (TTIP). The preparation of Y^{3+} and Mn^{3+} precursors and the gravimetrically determination of the precursors molality can be seen in Appendix B. 1.4 ml of TTIP was added to a stirred solution containing 0.03 mole of citric acid (CA) and 1 dl distilled water in a small beaker. A 5 ml syringe with a glass tube attached by a tight rubber tube, see Figure 3.2, was used to suck up TTIP liquid and deliver it to the beaker.



Fig. 3.2: Syringe with a leakage proof attached glass tube.

To avoid hydrolyzation, argon gas was flushed into the syringe before start, and during the delivery argon gas was flushed to the tip of the glass tube all the way to the CA solution. Some of the TTIP hydrolyzed when it came in contact with the solution, but after 1 h of stirring (440 rpm) on a hotplate with a temperature of 60 °C, the solution became blank, and all TTIP was solved in the CA solution. The cation precursors was held into a 2 L beaker and ethylene glycol (ET) was added. The molar ratio used between CA and ET was 1:1. The beaker was placed on a hotplate with a temperature of 150 °C and stirred (500 rpm) with a magnet until the gel had formed. A list of the content in the solution is presented in Table 3.3.

Tab. 3.3: The content of the solution forming $\text{YMn}_{0.85}\text{Ti}_{0.15}\text{O}_3$ gel

Y^{3+} precursor	Mn^{3+} precursor	TTIP	CA_{total}	Ethylene glycol	Amount of $\text{YMn}_{0.85}\text{Ti}_{0.15}\text{O}_3$
0.0315 mol	0.0267 mol	0.00470mol	0.780 mol	0.780 mol	0.0315 mol
721 g	621 g	1.40 ml	361 g	105 g	6.04 g

Chapter 3: Experimental

The gel was dried at 140 °C for 12 hours in a drying cabinet, before it was slowly heated to 200 °C for 3 hours to make it possible to extract the gel into a crystallization bowl, without breaking the beaker. The amount of the gel was about a third of the volume of the bowl. The dried gel was calcined in a crystallization bowl with the temperature program described in Figure 3.3. An overview of the whole citric acid method used in this chapter can be viewed in the flowchart in Figure 3.4. Calcined powder was then annealed in air at 800 °C for 2 hours to become nanocrystalline. The powder was characterized by XRD before and after annealing.

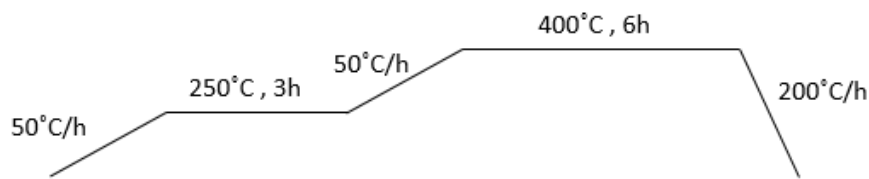


Fig. 3.3: Temperature program for calcination of the $\text{YMn}_{0.85}\text{Ti}_{0.15}\text{O}_3$ gel.

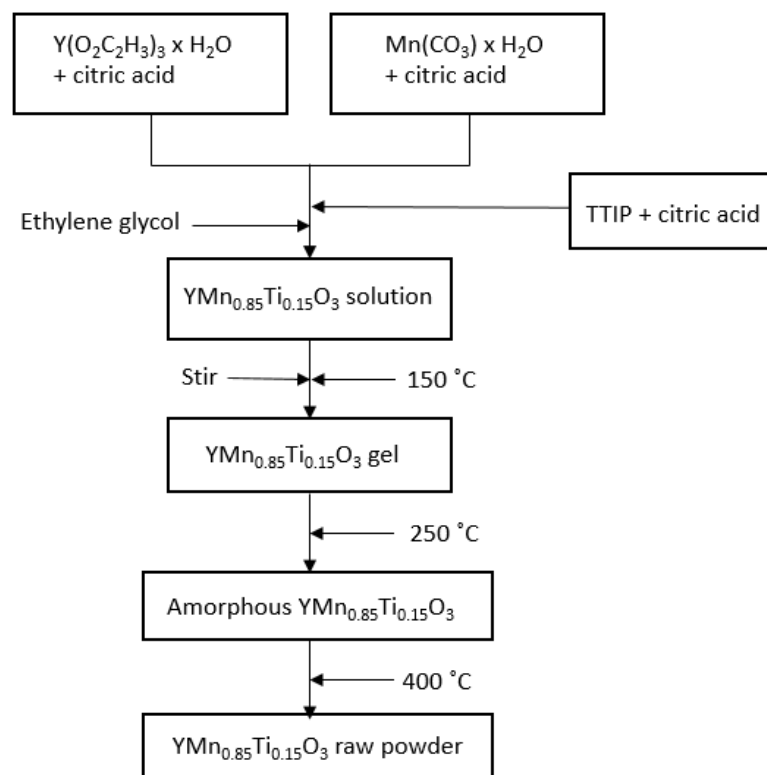


Fig 3.4: Flowchart over the citric acid method used to prepare nanocrystalline $\text{YMn}_{0.85}\text{Ti}_{0.15}\text{O}_3$ powder

3.1.3 Deposition of the active layer by dip coating

To limit the deposition of the dense functional layer to one side, the porous supports were attached to glass plates using liquid latex. A layer of liquid latex was smeared between the glass plate and the support, on the sides and a thin layer was deposited around the edges on the top surface. After solidification of the latex, a solution containing 0.626 g nanocrystalline $\text{YMn}_{0.85}\text{Ti}_{0.15}\text{O}_3$ powder and 22.5 ml ethanol was made (0.027g/ml). The nanocrystalline powder was sieved (100 μm) prior to limit agglomerates. To ensure randomly distributed particles and to avoid sedimentation during the dip coating, the solution was ultra-sonified for 1 min before each round of coating. A functional layer was deposited by dipping the glass plates with porous supports into the solution for 5 seconds. The membranes were drying for 10 min in room temperature, before the next layer was deposited (double coated). The first membrane that was made (P1) was triple coated, while the second membrane (P2) was double coated. Before sintering, membranes were dried for 1 hour in room temperature and carefully removed from the latex and the glass plates. An overview of sintering temperatures, sintering hours and number of deposited layers on each membranes are given in Table 3.4.

Tab. 3.4: Overview of the asymmetric membranes giving number of dip coatings, sintering temperature, sintering time and atmosphere.

Porous substrate sample	Number of dip coatings	Sintering temperature [°C]	Time [h]	Atmosphere
P1	3	1200/1400	2/1	Air
P2	2	1400	1	Air

3.2 Characterization of the powder

3.2.1 Structure and composition by x-ray diffraction

X-ray diffraction were used to characterize the powder by using BRUKER D8 ADVANCE DAVINCI with $\text{Cu K}\alpha$ radiation. Most of the diffractograms were scanned for 4 hours with a 2θ range of $14-110^\circ$ and a linear angle of 0.3° . A shorter scan for 30 min with a 2θ range of $14-75^\circ$ where mainly used to have control of the synthesis, while longer scans was used to find structural parameters. DIFFRAC.EVA V 3.0 was used to match the XRD paths to PDF cards.

3.2.2 Structure and composition analysis by Rietveld and Pawley method.

The analysis of XRD paths were done in Bruker AXS Topas-academic software version 4.2. The XRD path of YMnO_3 , porous support (P2) and nanocrystalline $\text{YMn}_{0.85}\text{Ti}_{0.15}\text{O}_3$ were refined for unit cell parameters, atomic positions in the unit cell, background and sample displacement. An overview of instrument and correction settings are seen in Table. 3.5. Both the low

Chapter 3: Experimental

temperature - and high temperature phase for hexagonal YMnO_3 were used as starting values in the Rietveld refinement. The starting values for unit- and atomic positions are obtained from Gibbs et.al[27] and can be seen in Table 3.6 and Table 3.7 for space group $P6_3cm$ and $P6_3/mmc$ respectively. A figure showing the different atom sites in space group $P6_3cm$ is seen in Appendix A.

XRD diffractograms of $\text{Y}_{1+x}\text{MnO}_3$ for $x=-0.05$ to $x=-0.30$, were only refined for unit cell parameters, background and sample displacement (Pawley method), due to the anisotropic tension in Y deficiency samples making it hard to fit all the intensities of the peaks. An hkl phase with space group $P6_3cm$ was used with the same unit cell parameters, instrument – and corrections settings as for the Rietveld analysis.

Tab. 3.5: Instrument and correction settings for Bruker AXS Topas-academic software version 4.2.

Parameter	Value
Primary radius/Secondary radius	280 mm/280 mm
2θ angular range of LPSD	3° *
FDS angle	0.3° *
Linear PSD Sample length	20 mm*
Source length	12 mm
Sample length	15 mm
Receiving slit length	12 mm
Primary/secondary soller	2.5°
N Beta	30
LP factor	0
Background	7

*These parameters varies with a short scan of 30 min.

Tab. 3.6: Structural parameters within space group $P6_3cm$. The unit cell parameters are $a = 6.14151(9)$ Å and $c = 11.4013(2)$ Å. Data is taken from Gibbs et al.[27].

Atoms	Np	x	y	z
Y1	2	0	0	0.2728(5)
Y2	4	1/3	2/3	0.2325(4)
Mn	6	0.3177(9)	0	0
O1	6	0.3074(4)	0	0.1626(4)
O2	6	0.6427(3)	0	0.3355(4)
O3	2	0	0	0.4744(6)
O4	4	1/3	2/3	0.0169(5)

Tab. 3.7: Structural parameters within space group $P6_3/mmc$. The unit cell parameters are $a=3.618961(15)$ Å and $c = 11.34090(9)$ Å. Data is taken from Gibbs et al.[27]

Atoms	Np	x	y	z
Y1	2	0	0	0
Mn	2	1/3	2/3	1/4
O1	2	0	0	1/4
O2	4	1/3	2/3	0.08557(7)

3.2.3 Microstructure

The cross section and the surface of the asymmetric membranes was examined with scanning electron microscope (SEM). The SEM micrographs were made on a Hitachi S-3400N using a Rhodium electron- source with SE and BSE detector. Applied voltage was 20 kV and SE was used to obtain the SEM micrographs. The membranes were attached to the sample holder using a double-sided sticky carbon tape. Prior to SEM, were the membranes divided in two, polished with grade # 800 and grade #1200 silicon carbide griding paper, before they were washed in ethanol and ultra-sonfied for 3 min. The polished cross –section was dried in a drying chamber in 10 min. Since the material is conductive, it was not necessary to coat the samples with gold or carbon.

3.3 Affect by atmosphere on unit cell parameters in yttrium deficient $YMnO_3$

To see how the unit cell parameters change in inert (N_2) and oxidizing (O_2) atmospheres, powders of $Y_{1+x}MnO_3$ for $x= -0.05$ to $x= -0.30$, prepared by solid state synthesis were placed in each their alumina crucibles and heated in a tube furnace with N_2 atmosphere. A characterization of the heated samples by x-ray diffraction were performed shortly after. The samples were then heated in O_2 atmosphere, with a slow cooling rate. Figure 3.5 represents the temperature program in both N_2 and O_2 atmosphere.

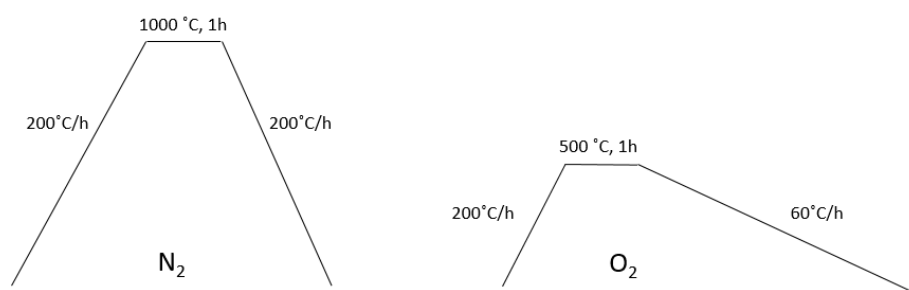


Fig. 3.5: Temperature program used for heating the Y deficient samples of $YMnO_3$ in N_2 (left) and O_2 (right) atmosphere.

Chapter 3: Experimental

3.4 Mass change in YMnO_3 and $\text{Y}_{0.80}\text{MnO}_3$ in varying atmosphere

Thermogravimetric analysis (TGA) of YMnO_3 and $\text{Y}_{0.80}\text{MnO}_3$ were performed using a Jupiter Netzsc STA 449C. The same temperature program was used for both samples, as seen in Figure 3.6. A more detailed program of the different stages and dwell times can be seen in Appendix F. Two different backgrounds were obtained by performing the measurement according to the program with an empty alumina crucible in nitrogen and oxygen. To obtain a good result, the background scan was subtracted from the sample scan. Gas flow rate of the aperture was set to 30 ml/min.

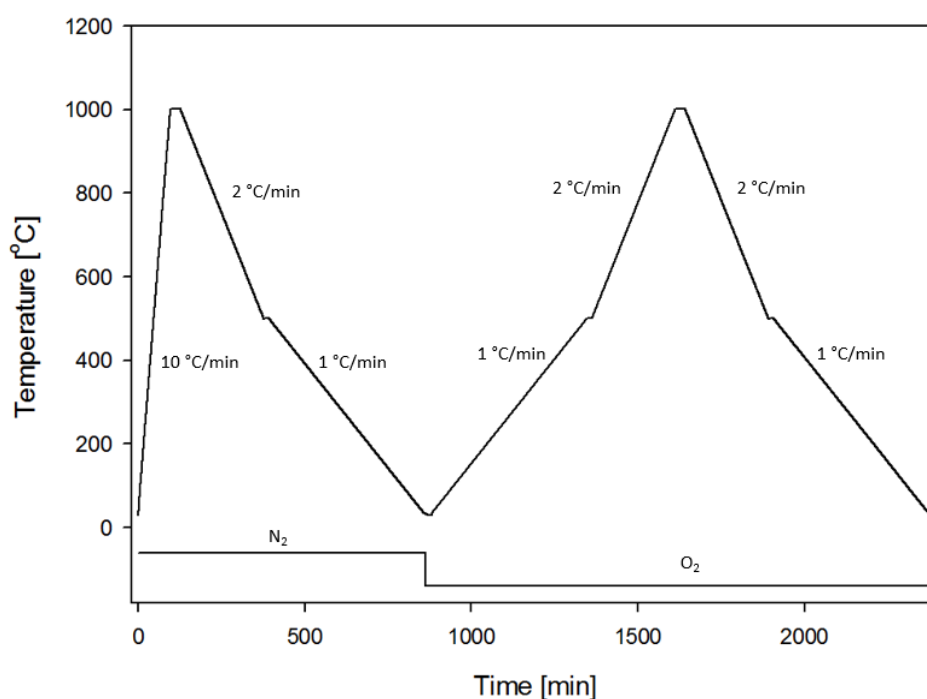


Fig. 3.6: Temperature and time program for the TGA analysis on YMnO_3 and $\text{Y}_{0.80}\text{MnO}_3$.

4. Results

4.1 Structure and characterization of YMnO_3 and yttrium deficient YMnO_3 powder

The x-ray diffraction pattern of bulk YMnO_3 made from general solid state synthesis was matched PDF card 04-011-9577 for space group $P6_3cm$ using Diffrac Eva, and can be seen in Appendix D. Phase pure bulk YMnO_3 is further used in the next XRD diagrams to compare Y deficient YMnO_3 samples, including the active layer and porous supports to space group $P6_3cm$. Refined structural parameters of bulk YMnO_3 within space group $P6_3cm$ are given in Table 4.1. The high uncertainty of the oxygen positions in Table 4.1 is because of the weak scattering of oxygen. The refinement gave unit cell parameters $a=6.1398(3)$ Å and $c=11.3990(2)$ Å, and a goodness of fit (R_{wp}) of 8.162. The Rietveld refinement (difference between experimental and calculated values) of bulk YMnO_3 is seen in Appendix D.

Tab. 4.1: Structural parameters obtained from refined diffractogram of YMnO_3 made from solid state synthesis within space group $P6_3cm$. The unit cell parameters are $a=6.1398(3)$ Å and $c=11.3990(2)$ Å. The refinement gave $R_{wp}=8.162$.

Atoms	Np	x	y	z
Y1	2	0	0	0.283(7)
Y2	4	1/3	2/3	0.242(7)
Mn	6	0.333(7)	0	0
O1	6	0.30(1)	0	0.159(4)
O2	6	0.643(9)	0	0.336(2)
O3	2	0	0	0.47(5)
O4	4	1/3	2/3	0.022(5)

4.1.1 Structural analysis of $\text{Y}_{1-x}\text{MnO}_3$ by x-ray diffraction and refined unit cell parameters by Pawley method

X-ray diffractograms of yttrium deficient samples as prepared from solid state synthesis reveals a high degree of freedom of the cation R/Mn ratio. From $\text{Y}_{0.85}\text{MnO}_3$ some weak reflections appear at 18° , 32.5° and 58.6° 2θ that increase in intensity with increased Y deficiency. This new emerging phase was identified as Mn_3O_4 (hausmannite) with trigonal structure. The most pronounced intensities from this new emerging phase are labelled by a star in Figure 4.1. In the lower end of Figure 4.2, a better view of the shift towards higher 2θ for the Bragg reflections from the (110), (111) and (112) planes is seen with increased yttrium deficiency. The same shift towards right can be seen for the Bragg reflection belonging to the (004) plane. There is not observed any pronounced broadening of peaks with increased yttrium deficiency.

Pawley method of the x-ray diffractograms show that both the a and c unit cell parameters decrease slightly as the yttrium content in the samples decreases, which coincide with the shift of intensities found in Figure 4.1. The refined unit cell parameters in yttrium deficient YMnO_3 in both air (as prepared), N_2 - and O_2 atmospheres are represented in Figure 4.2. There is a trend in higher goodness of fit (R_{wp}) with increasing yttrium deficiency for as prepared samples, seen in Table. 4.2. This is mainly attributed to intensity problems. These intensity problems is more pronounced with Rietveld analysis compared to Pawley fitting, and Pawley method is therefore chosen to give the best fit of the x-ray diffractograms. There is observed a slight degree of broadening with increased yttrium deficiency, but this was not as pronounced as the intensity problems. The abnormal bad fitting seen for $\text{Y}_{0.95}\text{MnO}_3$ and $\text{Y}_{0.90}\text{MnO}_3$ is due to large grain sizes. These samples are not taken into consideration when evaluating trends in the unit cell parameters. This also applies for $\text{Y}_{0.70}\text{MnO}_3$ that experienced peritectic decomposition during sintering.

A higher goodness of fit is obtained for yttrium deficient YMnO_3 heated in N_2 and O_2 atmospheres compared to as prepared yttrium deficient samples. A problem with broadening during Pawley method was more pronounced for these samples compared to as prepared yttrium deficient YMnO_3 . This broadening is not easy to see in the x-ray diffractograms for yttrium deficient samples annealed in N_2 and O_2 atmospheres, which can be seen in Appendix E. The x-ray diffractograms of yttrium deficient samples heated in N_2 and O_2 atmospheres also reveals the same high degree of freedom of the cation R/Mn ratio, before reflections appears from Mn_3O_4 (hausmannite) around $\text{Y}_{0.85}\text{MnO}_3$ up to $\text{Y}_{0.70}\text{MnO}_3$. With increased yttrium deficiency in YMnO_3 for samples heated in N_2 , a slight shift towards higher 2θ values for the Bragg reflections belonging to the (110), (111) and (112) planes, while the Bragg reflection belonging to the (004) plane does not change. In yttrium deficient YMnO_3 samples heated in oxidizing atmosphere a shift towards higher 2θ is seen for the Bragg reflection related to the (004) plane, while the Bragg reflections related to the (110) and (111) does not change with increased yttrium deficiency.

Tab. 4.2: Goodness of fit (R_{wp}) values from Pawley fitted x-ray diffractograms of yttrium deficient YMnO_3 made from solid state synthesis.

Composition	R_{wp} values		
	Air (as prepared)	N_2 atmosphere	O_2 atmosphere
YMnO_3	7.301	-	-
$\text{Y}_{0.95}\text{MnO}_3$	11.047	13.336	12.780
$\text{Y}_{0.90}\text{MnO}_3$	14.072	14.492	16.745
$\text{Y}_{0.85}\text{MnO}_3$	8.875	11.778	9.645
$\text{Y}_{0.80}\text{MnO}_3$	10.137	12.285	10.860
$\text{Y}_{0.75}\text{MnO}_3$	11.070	13.844	12.108
$\text{Y}_{0.70}\text{MnO}_3$	17.404	15.441	15.739

Chapter 4: Results

After heat treatment in inert atmosphere (N_2), the a unit cell parameter decreases for all the yttrium deficient samples, which the c unit cell parameter increases. The opposite is true for powders annealed in oxidizing atmosphere (O_2), where the unit cell parameter a increase, while unit cell parameter c has a slight decreases with increased yttrium deficiency in $YMnO_3$. The arrows in Figure 4.2 is a guide to the eye to get a better view of the trends in the unit cell parameters in different atmospheres.

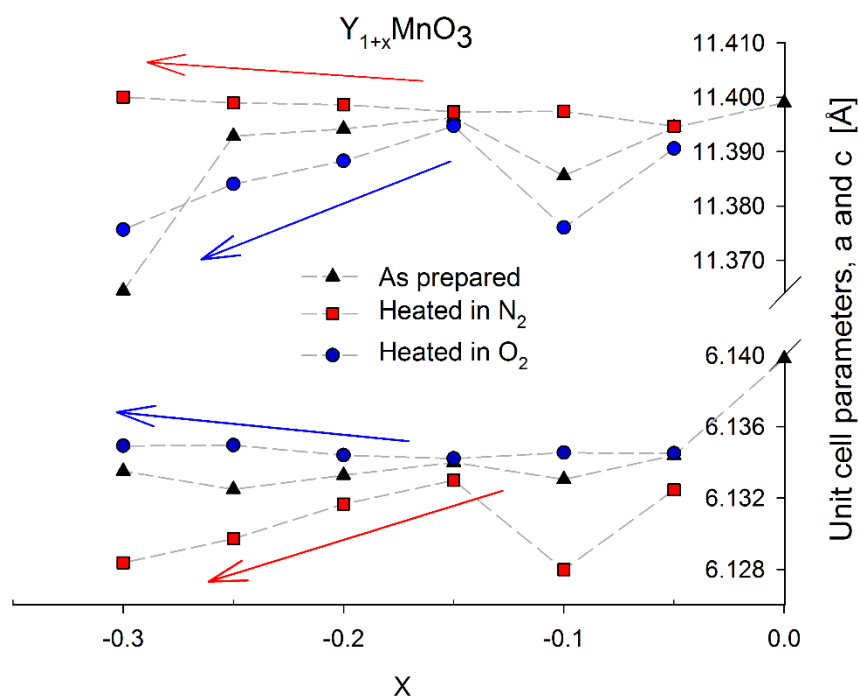


Fig. 4.2: Unit cell parameters a and c for varying yttrium deficiency in $YMnO_3$, in both as prepared in air (black), N_2 (red) and O_2 (blue) atmospheres, obtained by Pawley method. The arrows are a guide to the eye, to see the trends more clearly

A decrease in unit cell volume is seen with increased Y deficiency for all powders prepared in both air, N_2 and O_2 atmospheres. The unit cell volume and the c/a ratio is seen in Figure 4.3. In oxidizing atmosphere the c/a ratio decreases with less Y in the structure, while it is opposite in inert atmosphere where the c/a ratio increases.

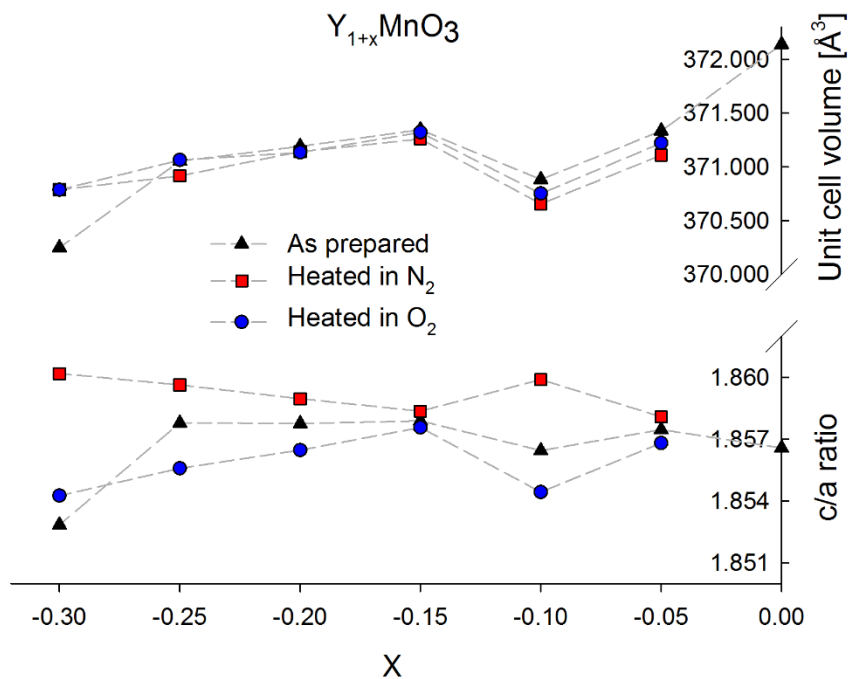


Fig. 4.3: Unit cell volume and c/a ratio for varying yttrium deficiency in $YMnO_3$, in both as prepared in air (black), N_2 (red) – and O_2 (blue) atmospheres, obtained by Pawley method.

4.2 Mass change of $YMnO_3$ and $Y_{1+x}MnO_3$ ($x < 0$) with varying conditions

Thermogravimetric analysis (TGA) show that upon heating in O_2 and N_2 atmosphere and an anomalously behavior is seen for both $YMnO_3$ and $Y_{0.80}MnO_3$. Upon heating in O_2 atmosphere, $YMnO_3$ experience an increase followed up by an abnormal and substantial mass loss after 800°C . $Y_{0.80}MnO_3$ experience a strange increase in oxygen content around 700°C in oxidizing atmosphere. This together with the choppy behavior seen for $Y_{0.80}MnO_3$ in N_2 cannot be explained. TGA graphs for both $Y_{0.80}MnO_3$ and $YMnO_3$ in O_2 and N_2 atmosphere is shown in Figure 4.4 and Figure 4.5 respectively. A reversible oxygen adsorption is found during cooling for $Y_{0.80}MnO_3$ and $YMnO_3$ in oxidizing atmosphere. The calculated oxygen content (δ) for both powders is left to the discussion, as there is no obvious temperatures for the compounds to be stoichiometric. Oxygen content is not calculated upon heating, because of the strange behaviors as mention above.

Chapter 4: Results

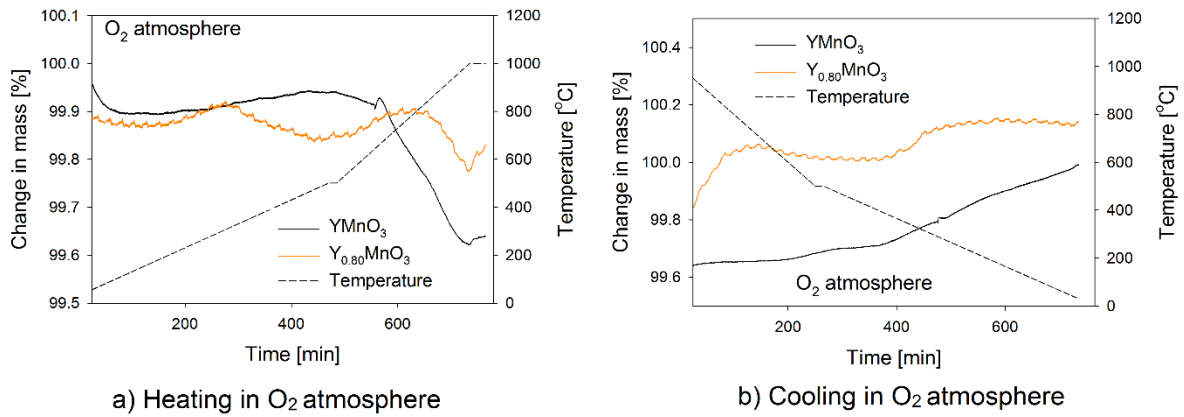


Fig. 4.4: Thermogravimetric data showing mass loss/gain and temperature as a function of time in O_2 atmosphere upon a) heating and b) cooling.

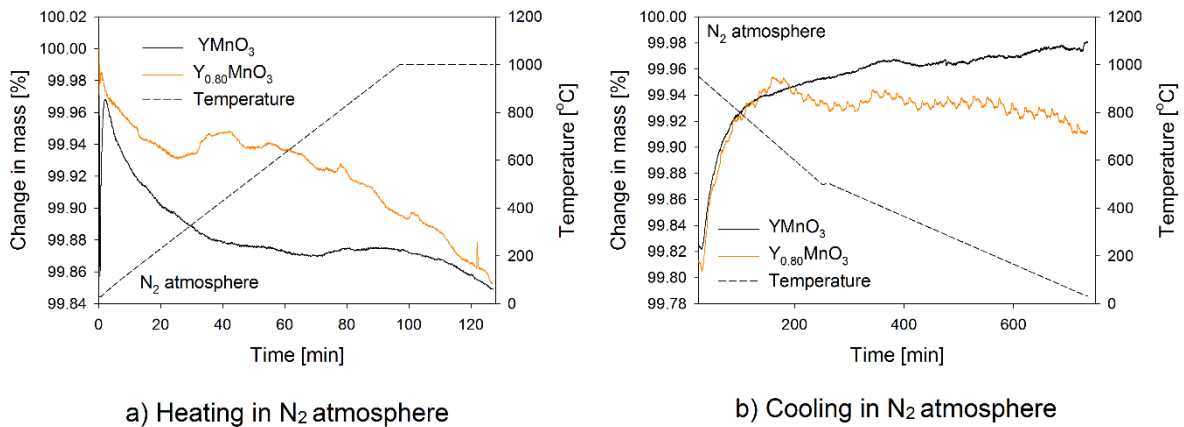


Fig. 4.5: Thermogravimetric data showing mass loss/gain and temperature as a function of time in N_2 atmosphere upon a) heating and b) cooling.

4.3 Structural analysis of the asymmetric membrane

4.3.1 Structure and composition of porous support of $YMn_{0.85}Ti_{0.15}O_3$ prepared by solid state synthesis

The addition of carbon black gave successfully porous materials, and the densities and % of crystallographic density compared to $YMnO_3$ are given in Tab. 4.3. The crystallographic density of $YMnO_3$ was found to be 5.132 g/cm^3 .

Tab. 4.3: Crystallographic density, density of the pellets and sintering atmospheres for the two porous support P1 and P2.

Porous substrate sample	Sintering atmosphere	Density [g/cm ³]	% of crystallographic density
P1	Air/N ₂	2.1358	41.62
P2	N ₂	2.0220	39.39

Both the substrates were slightly skewed after sintering. This bias originates from the uniaxial pressing as pressure gradients easily can occur, especially with a 30 mm diameter on the pressing tool.

The porous support P1 made by solid state synthesis, was not phase pure after first sintering in air, and some of the reflections belonging to the secondary phase was matched a PDF card belonging to yttrium oxide (Y₂O₃), while the rest was not identified. It was however not matched with an orthorhombic structure. After a second firing in N₂ the porous support became phase pure. The x-ray diffractograms of the porous support P1 fired once in air and reheated in N₂ is seen in Appendix C. A displacement of the reflections towards lower 2θ values is observed for the phase pure titanium substituted sample compared to pure YMnO₃. This displacement has occurred because of a height difference when preparing the samples prior to XRD scans. A posteriori displacement correction of the data, reveals a displacement of the (004) reflection towards higher 2θ values, while the reflections from the (110), (111) and (112) planes are still displaced towards lower 2θ values.

The same shift of the Bragg reflections is also seen for the porous support P2, in Figure 4.6. This sample was phase pure after one sintering in N₂. In both XRD scans of the porous supports a decrease in peak intensity together with an increase in peak broadening is observed compared to YMnO₃ sample.

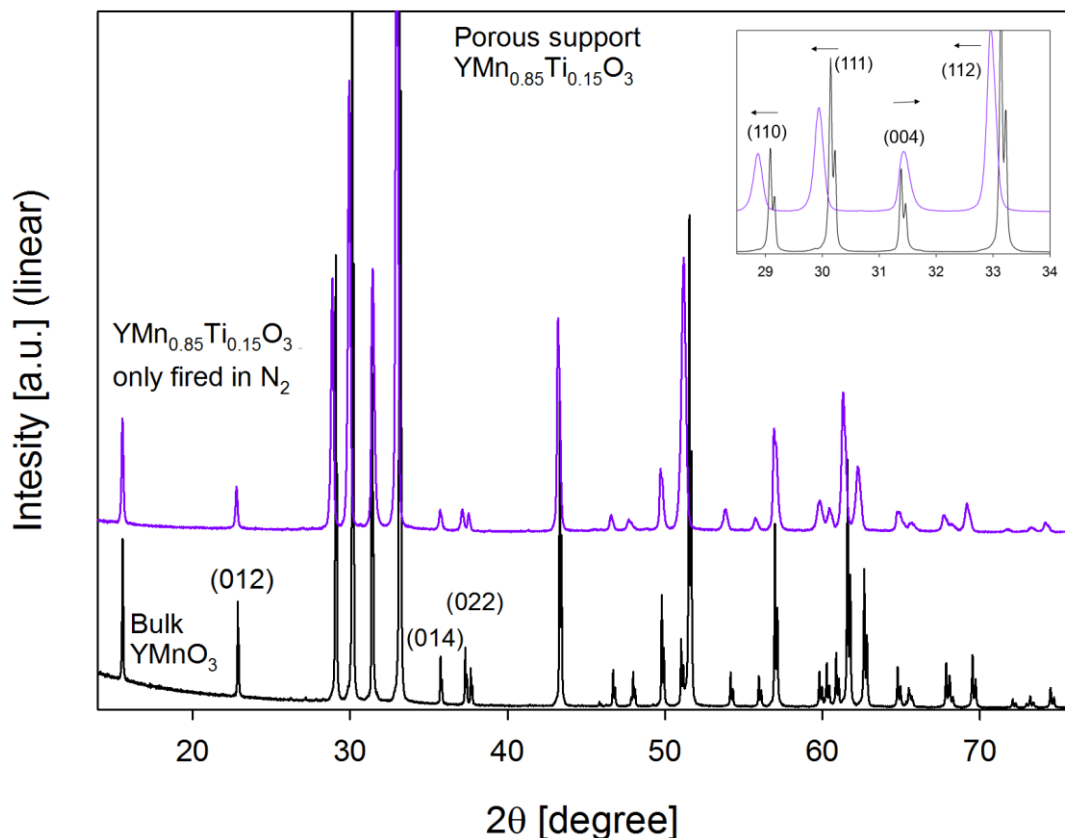


Fig. 4.6: X-ray diffractograms of the porous support (P2) of $\text{YMn}_{0.85}\text{Ti}_{0.15}\text{O}_3$ sintered in N_2 (purple). The x-ray diffractogram is compared to pure YMnO_3 within space group $P6_3cm$ made from general solid state synthesis. An excerpt of the (110), (111), (004) and (112) reflections with a smaller range of 2θ values is inserted in the top-right corner of the figure to give a better view of the displacements.

Refined structural parameters and unit cell parameters of the porous support P2 within space group $P6_3cm$, are seen in Table 4.4. Rietveld analysis was not performed on the x-ray diffractogram of the porous support P1 (seen in Appendix C), as both samples comes from the same powder. In Table 4.4, the unit cell parameters and structural parameters of the porous support P2 are compared to bulk YMnO_3 made by solid state synthesis. Unit cell parameter a for porous support P2 increases, while the unit cell parameter c decreases compared to bulk YMnO_3 . The Refined x-ray diffractogram of the porous support P2, can be seen in Appendix D.

Tab. 4.4: Structural and unit cell parameters obtained from refined diffractograms of porous support P2 ($\text{YMn}_{0.85}\text{Ti}_{0.15}\text{O}_3$) and YMnO_3 made from solid state synthesis within space group $P6_3cm$.

	YMnO_3	$\text{YMn}_{0.85}\text{Ti}_{0.15}\text{O}_3$ (P2)
R_{wp}	8.162	15.876
a [\AA]	6.1398(3)	6.1778(1)
c [\AA]	11.3990(2)	11.367(2)
V [\AA^3]	372.14(4)	375.7(1)
Y1 z	0.283(7)	0.27(4)
Y2 z	0.242(7)	0.23(8)
Mn x	0.333(7)	0.33(5)
O1 x	0.30(1)	0.29(5)
O1 z	0.159(4)	0.16(3)
O2 x	0.643(9)	0.65(3)
O2 z	0.336(2)	0.34(0)
O3 z	0.47(5)	0.48(9)
O4 z	0.022(5)	0.02(4)

4.3.2 Structure and composition of nanocrystalline $\text{YMn}_{0.85}\text{Ti}_{0.15}\text{O}_3$ prepared by citric acid method.

Nanocrystalline powder of $\text{YMn}_{0.85}\text{Ti}_{0.15}\text{O}_3$ made by citric acid method was made to avoid sedimentation during the deposition of the active layer on top of the porous support, and to obtain a dense functional layer. Pure hexagonal nanocrystalline powder of $\text{YMn}_{0.85}\text{Ti}_{0.15}\text{O}_3$ was obtained, and is shown in Figure 4.7 together with bulk YMnO_3 prepared by solid state synthesis for comparison. Titanium substitution gives a phase transition from $P6_3cm$ to $P6_3/mmc$, especially evidenced by the disappearance of the (012) and (022) super reflections marked by arrows in Figure 4.7. Reflection broadening is also observed for the entire range of reflections in nanocrystalline powder of $\text{YMn}_{0.85}\text{Ti}_{0.15}\text{O}_3$ compared to bulk YMnO_3 . The Bragg reflections from the (110) and (111) planes have a pronounced shift to lower 2θ values compared to YMnO_3 , and the Bragg reflection from the (004) plane shift towards higher 2θ values.

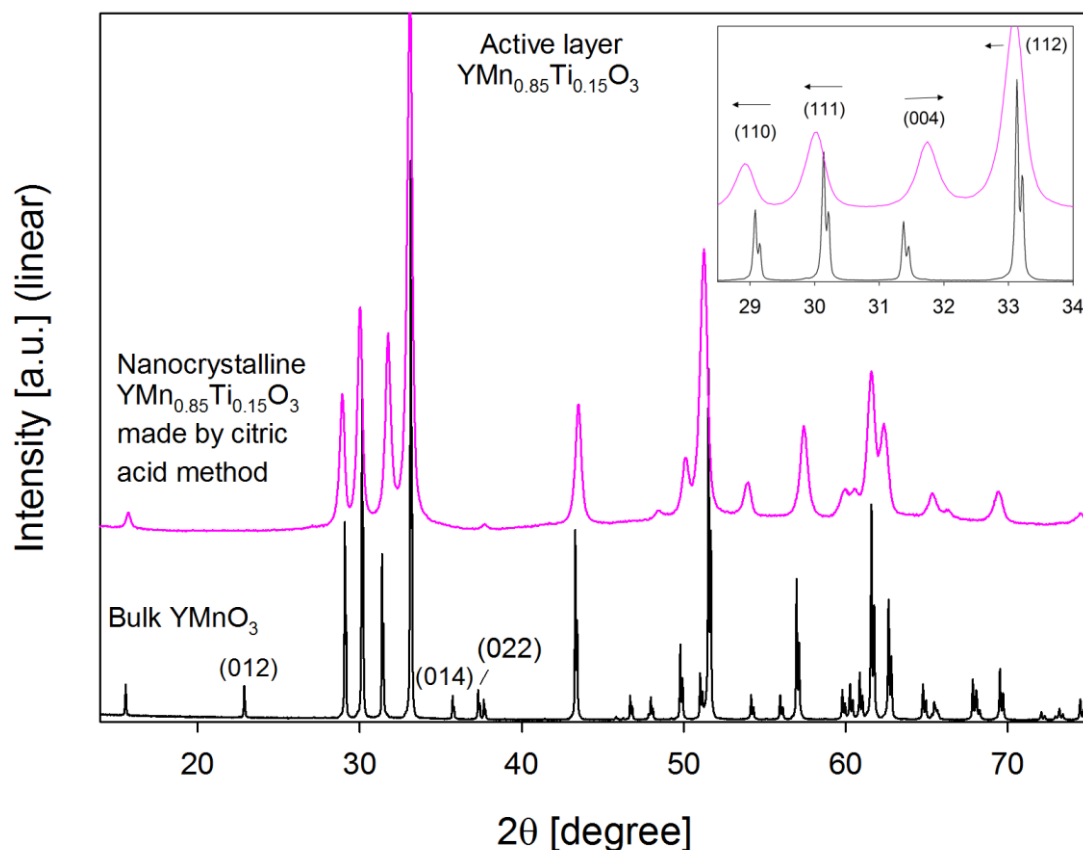


Fig. 4.7: X-ray diffractogram of hexagonal nanocrystalline $\text{YMn}_{0.85}\text{Ti}_{0.15}\text{O}_3$ within space group $P6_3/mmc$ compared to bulk hexagonal YMnO_3 with space group $P6_3cm$. An excerpt of the (110), (111), (004) and (112) reflections with a smaller range of 2θ values is inserted in the top-right corner of the figure to give a better view of the displacements.

The unit cell parameters a and c , as well as structural parameters for nanocrystalline $\text{YMn}_{0.85}\text{Ti}_{0.15}\text{O}_3$ were found by Rietveld analysis. The XRD pattern was refined within space group $P6_3/mmc$ and gave refined unit cell parameters of $a = 3.565(0)$ Å and $c = 11.26(6)$ Å. Structural parameters from Rietveld refinement of the x-ray diffractogram of the active layer of $\text{YMn}_{0.85}\text{Ti}_{0.15}\text{O}_3$ is seen in Table 4.5, and the Rietveld refinement can be seen in Appendix D. The only atom position released is the z direction of the O2, because this site is not in high symmetric position. The refinement did not yield an adequately fit to the experimental XRD graph, illustrates by the high goodness of fit of 18.045. One of the main reasons for this is due to restriction in Topas, which does not take into account anisotropic strain the material experience during Ti substitution on Mn site. The crystallite size of nanocrystalline $\text{YMn}_{0.85}\text{Ti}_{0.15}\text{O}_3$ was found to be 36.1 ± 3 nm.

Tab. 4.5: Structural parameters obtained from refined diffractogram of nanocrystalline $\text{YMn}_{0.85}\text{Ti}_{0.15}\text{O}_3$ prepared by citric acid method within space group $P6_3/mmc$. The lattice parameters are $a=3.565(0)$ Å and $c=11.26(6)$ Å. The refinement gave $R_{\text{wp}}=18.045$.

Atoms	Np	x	y	z
Y1	2	0	0	0
Mn	2	1/3	2/3	1/4
Ti	2	1/3	2/3	1/4
O1	2	0	0	1/4
O2	4	1/3	2/3	0.08(8)

4.4 Microstructure of porous support and active layer of the membrane

The active layers of nanocrystalline $\text{YMn}_{0.80}\text{Ti}_{0.15}\text{O}_3$ was not dense after sintering. The porous support also as expected became denser after sintering. An overview of the surface of the porous support and active layer is seen in Figure 4.8 for both the double coated and triple coated membranes. It is observed that the porous supports are denser compared to the active layer. The double coated and the triple coated membranes had also almost the same membrane thickness of 25 µm and 25.5 µm, seen in Figure 4.9, showing the cross sections of the membranes.

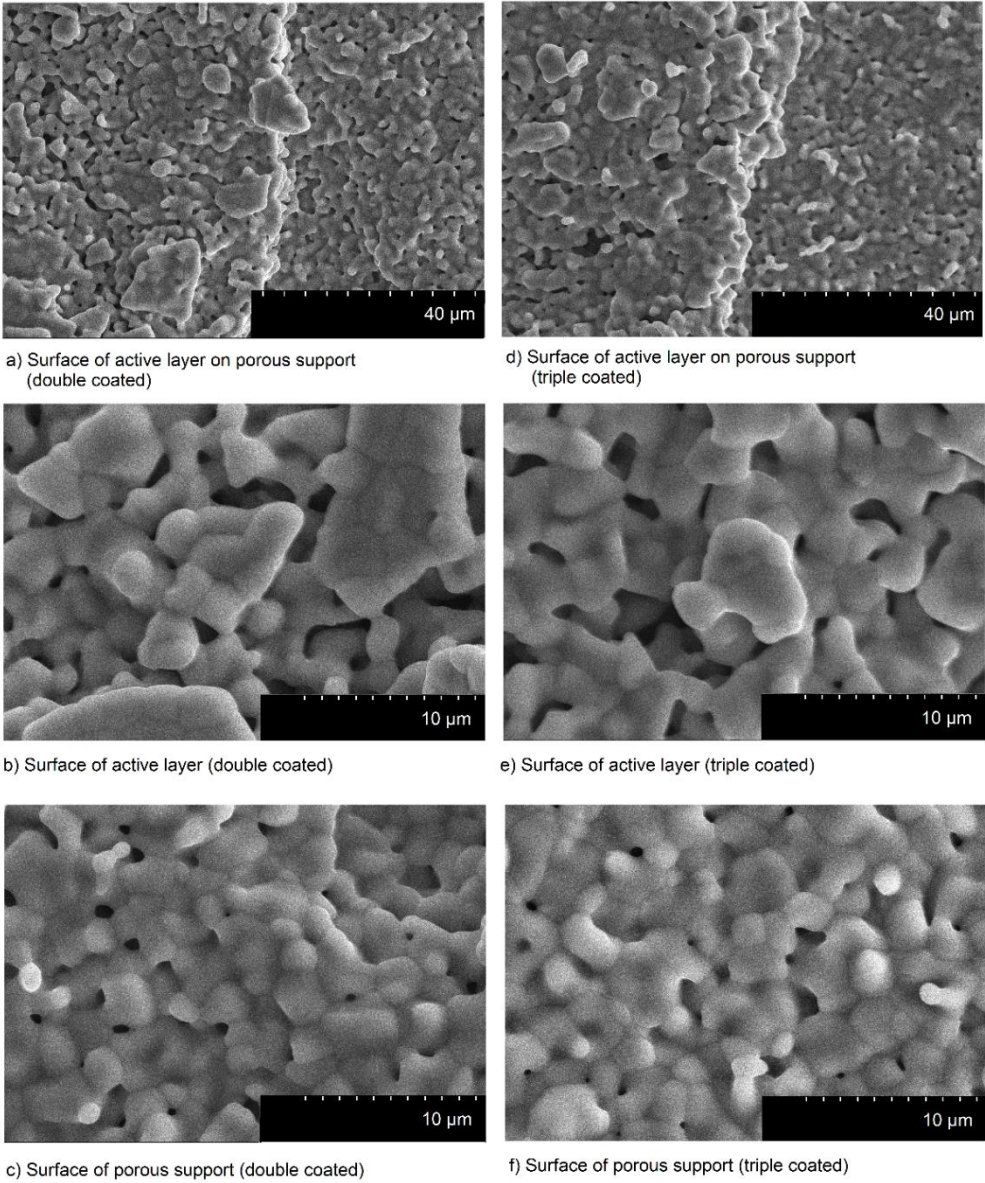
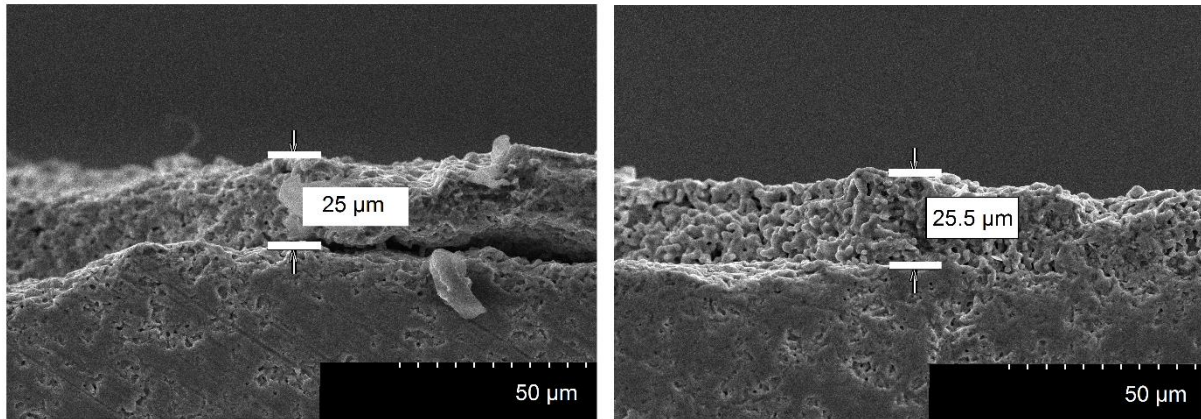


Fig. 4.8: SEM micrographs from the surface of both active layer and porous support of the sintered asymmetric membranes.



a) Cross section showing active layer on porous support (double coated).

b) Cross section showing active layer on porous support (triple coated).

Fig. 4.9: SEM micrographs showing the cross section of the sintered asymmetric membranes. Porous support dip coated a) 2 times and b) 3 times

5. Discussion

5.1 The influence of yttrium deficiency in YMnO_3 .

Yttrium deficiency in hexagonal YMnO_3 can be charge compensated by oxygen vacancies, which gives an oxygen poor structure, seen in (5.1) or they can be charge compensated by oxidation of a fraction of Mn^{3+} to Mn^{4+} as illustrated in (5.2).



It is important to know that these two possibilities are extremes, and that there might exist both oxygen vacancies and Mn^{4+} at the same time to charge compensate for the yttrium deficiency. The defect chemistry in stoichiometric YMnO_3 is not well known, and especially not for yttrium deficient YMnO_3 . The following sections provide a discussion about how reducing/oxidizing atmospheres influence the crystal structure, and suggest probable defect reactions that may arise in the material during different conditions.

5.1.1 Structure and solubility limit

All yttrium deficient samples were fired at 1723 K (1450 °C), indicating that we are in the $\beta\text{-Mn}_3\text{O}_4$ solubility region of h- YMnO_3 according to the estimated $\text{Y}_2\text{O}_3\text{-Mn}_2\text{O}_3$ pseudo-binary phase diagram[34]. Trace amounts of $\beta\text{-Mn}_3\text{O}_5$ appear in the as prepared x-ray diffraction pattern for $\text{Y}_{0.80}\text{MnO}_3$ and get more pronounced with a less degree of yttrium in the structure. The same trend is also seen for the yttrium deficient samples annealed in both N_2 and O_2 atmospheres. This clearly shows that the solid solubility region of $\beta\text{-Mn}_3\text{O}_4$ in yttrium deficient hexagonal YMnO_3 is extended more to the left in the phase diagram, seen as the dotted red line in Figure 5.1. Since there has not been sintered any yttrium deficient samples at lower temperatures, it is impossible to say what value the slope of curve will exhibit in the vertical direction (dotted orange line, Figure 5.1).

A degree of freedom in the Y/Mn ratio may explain the different unit cell parameters and phase transition temperatures found in literature for YMnO_3 . In addition, it is promising in terms of reducing the cost, but on the other hand, mechanical and chemical properties must be further investigated to see how less yttrium in the structure affects the material.

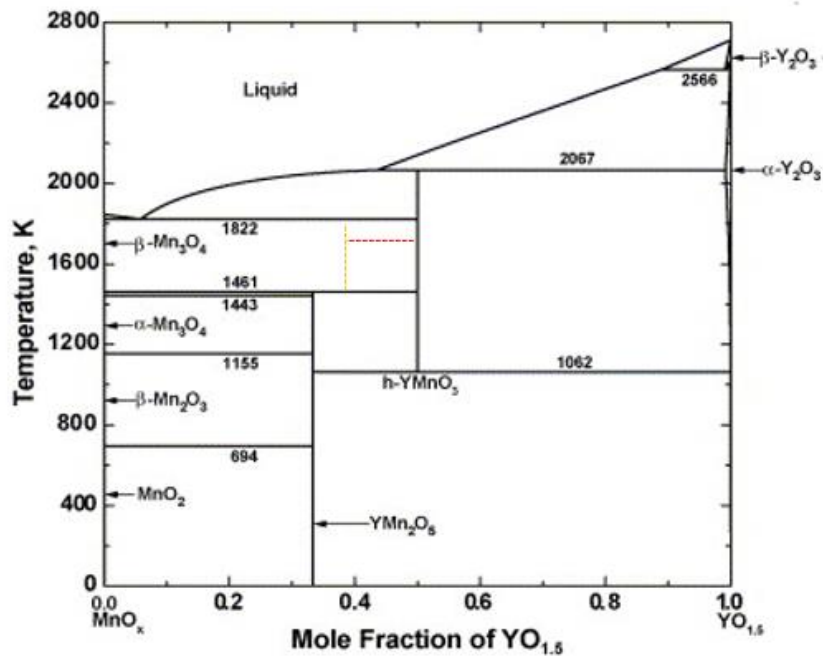


Fig. 5.1: A suggestion to a revised new solid solubility limit (dotted red line) of β - Mn_3O_4 in yttrium deficient $YMnO_3$ than first expected in the pseudo – binary phase diagram for the Y-Mn-O system. The orange dotted line is just an assumption of the slope of the curve (this has not been experimentally shown in this thesis). The originally figure is reprinted from Chen et.al [34]

The surprisingly high solid solubility region even with 15-20 % yttrium deficiency in $YMnO_3$ may be due to the layered structure of hexagonal $YMnO_3$. The conducting state in hexagonal $YMnO_3$ has been attributed to the overlap between the d-orbitals of Mn in the ab-plane[24]. There is less contact between the MnO_5 layers along the c direction, and it is therefore reasonable to believe that a removal of a Y-ion, which is situation between the layers, not will destabilize the structure.

Moreover, the peritectic decomposition observed for $Y_{0.70}MnO_3$ after sintering indicates that the peritectic decomposition line left in Figure 5.1 at 1822 K is shifted towards a lower temperature (~ 1723 K) for highly yttrium deficient samples.

5.1.2 Distortion of the unit cell with varying partial pressure of oxygen

For a higher degree of yttrium deficiency in $YMnO_3$ prepared in air atmosphere, see Figure 4.1, a shift toward higher 2θ values is observed for Bragg reflections associated with the high intensity (110), (111), (112) and (004) planes. A shift towards higher 2θ values indicates a decrease in the distance d_{hkl} between adjacent lattice planes. It is obvious that a change in d_{hkl} is related to a change in a- and c unit cell parameters. The high intensity Bragg reflections related to the a and c axis are illustrated in space group $P6_3cm$ in Figure 5.2. Decreased distance between adjacent planes for intensities related to the a and c axis indicates a compression of the hexagonal structure in both a and c direction.

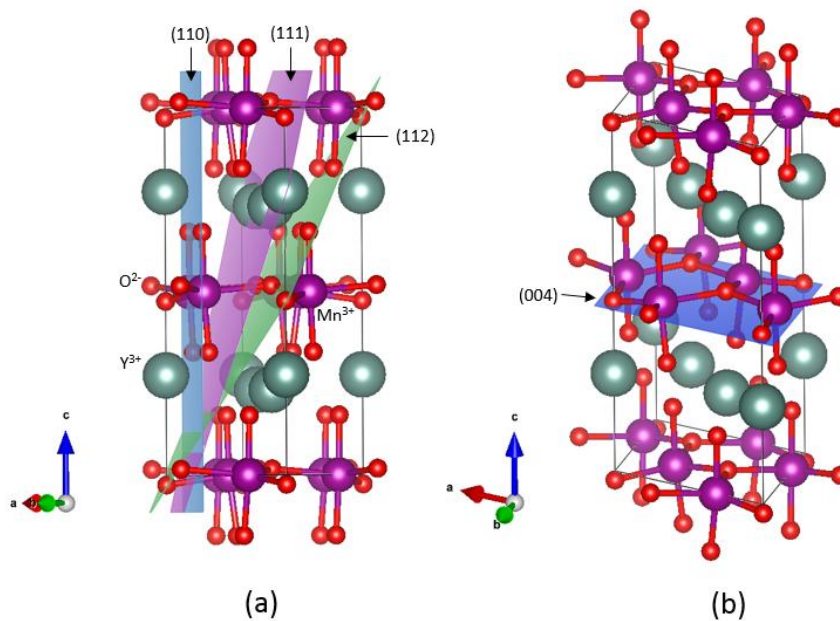


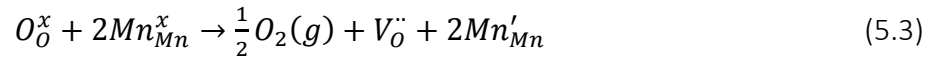
Fig 5.2: (a) A visualizing of the (110), (111) and (112) planes in hexagonal YMnO_3 with space group $P6_3cm$. All planes are dependent on direction a , being either perpendicular or having an angle α not being 0 with the a -direction. Decreased distance between adjacent planes will give a compression along a direction. (b) The (004) plane is perpendicular to the c -axis, and parallel to the a -axis. A decreased distance between adjacent planes gives a compression along c direction. The figure is made using VESTA software [26], with structural parameters from Gibbs et al. [27]

The same structural trend was found by Pawley fitted x-ray diffractograms of as prepared yttrium deficient samples, Figure 4.2. The refined unit cell parameters a and c , showed a slight decreased with increased yttrium deficiency, especially from $\text{Y}_{0.85}\text{MnO}_3$ to $\text{Y}_{0.75}\text{MnO}_3$. This indicates the same compression of the hexagonal unit cell in both ab plane and c -direction. The compression leads to a volume decrease and a slight increase in the c/a ratio compared to stoichiometric YMnO_3 . There is no obvious explanation for this behavior. However, yttrium deficiency in YMnO_3 can be charge compensated by oxygen vacancies or oxidation of a fraction Mn^{3+} to Mn^{4+} . A smaller radii of Mn^{4+} compared to Mn^{3+} may explain the compression of the unit cell when less yttrium is introduced.

Reducing condition for stoichiometric YMnO_3 will be attributed to oxygen leaving the material due to the partial pressure difference between the material and the surroundings. It is suggested by Overton et.al [43] that oxygen vacancies in YMnO_3 preferably will leave planar atom sites in the MnO_5 units. An expansion of the structure was also found in both a and c directions, followed up by a decline in the tilting of MnO_5 units with less oxygen in the structure of YMnO_3 . Less decline of MnO_5 bipyramids is also associated with less displacement of yttrium along c direction. Oxygen vacancies can be charge compensated by reduction of Mn^{3+} to Mn^{2+} ,

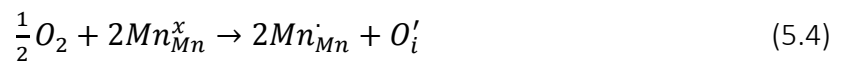
Chapter 5: Discussion

written in Kröger-Vink notation and is seen in equation (5.3), and since the ionic radius of Mn^{2+} is larger than Mn^{3+} , the volume of the unit cell will probably increase. The larger ionic radius of Mn^{2+} will also increase the average Mn-O bond length and thus the a-axis would be expected to increase.



It might seem reasonable to assume the same trends in yttrium deficient samples annealed in reducing atmosphere as for oxygen vacancies in stoichiometric $YMnO_3$. In fact, the opposite happens for unit cell parameter a which decrease, while unit cell parameter c slightly decreases with increased yttrium deficiency in $YMnO_3$. This behavior is also seen in the x-ray diffractograms of yttrium deficient $YMnO_3$ annealed in N_2 atmosphere, as a shift toward higher 2θ values is observed for intensities related to the (110), (111) and (112), while the intensity related to the (004) plane hardly shifts. A possible explanation can be that oxygen vacancies are preferably removed from the apical sites around MnO_5 , instead of the planar sites. A further reasonable discussion is limited on the basis of the obtained data.

For stoichiometric $YMnO_3$ annealed in oxidizing atmosphere it is expected that oxygen will go into the material from the atmosphere. At low temperatures, this oxygen adsorption is attributed to interstitial oxygen, as the hexagonal structure of $YMnO_3$ is less dense compared to the related perovskite phase. Interstitial oxygen can be charge compensated by oxidation of a fraction of Mn^{3+} to Mn^{4+} and is seen by the following Kröger-Vink notation



The position of the oxygen interstitial in the hexagonal structure is discussed in more details in an own section. A decreased c/a ratio for yttrium deficient samples of $YMnO_3$ annealed in oxidizing atmosphere is due to a compression along the c axis and an slight expansion along the a direction. Since oxygen interstitials is charge compensated by oxidation of Mn^{3+} to Mn^{4+} , one would probably expect the structure to be compressed in the planer plane because of the smaller radius of Mn^{4+} compared to Mn^{3+} . However, a reasonable explanation for this behavior cannot be conducted, and more attention has to be given to the position of the interstitial oxygen, and how this influence the structure.

Limitations of The Pawley fit

Not all calculated graphs found by Pawley fitting were able to yield a good fit to the experimental x-ray graphs of yttrium deficient $YMnO_3$. One of the reasons for this comes from the limiting factor the fitting program exhibits, which is that it assumes stoichiometric

compound when calculating the best fit. A higher degree of yttrium deficiency, gave a higher strain seen by the limiting fit. The strain is believed to be anisotropic, however the broadening of the intensity related to the (004) plane was not pronounced and it is therefore hard to say. The layered nature of the low temperature hexagonal phase is one of the reasons for the strain. The abnormally high goodness of fit values for $Y_{0.95}MnO_3$ and $Y_{0.90}MnO_3$ is attributed to large grain size which occurred during sintering. It is suggested that less yttrium in the structure will increase the diffusion distance in the structure, and hence it is believed that increased yttrium will give smaller grains. A decrease in the sintering temperature will also give smaller grains.

5.1.3 Oxygen storage ability

It was not clear where to assume stoichiometric compounds from the thermogravimetric data during heating. This applies especially for $Y_{0.80}MnO_3$ during heating, seen in Figure 4.4 and Figure 4.5. In O_2 atmosphere, the sudden increase in oxygen content around 600 °C for $Y_{0.80}MnO_3$ with a following decrease has no obvious explanation. This does also apply for the sudden decrease in oxygen content for $YMnO_3$ around the same temperature region. The excess oxygen is therefore only calculated during cooling in O_2 and N_2 atmosphere, as this behavior was more similar to what Remsen et.al[14] found for hexagonal manganites.

The assumption of stoichiometric compound during cooling was done where there was a high probability to only have Mn^{3+} in the structure. For $Y_{0.80}MnO_3$ in O_2 atmosphere this is seen as the plateau between 400°C – and 500°C, while for $YMnO_3$ in the same atmosphere is it assumed to be around 450 °C. For $YMnO_3$ and $Y_{0.80}MnO_3$ in N_2 atmosphere, stoichiometric compound is assumed to be around 400 °C and the plateau between 450-500 °C respectively. The excess oxygen content as a function of temperature for $YMnO_{3+\delta}$ and $Y_{0.80}MnO_{2.7+\delta}$ in both O_2 and N_2 atmosphere is shown in Figure 5.3 and Figure 5.4 respectively. For the excess oxygen calculations in $Y_{0.80}MnO_3$ it was assumed that less yttrium in the structure was charge compensated by oxygen vacancies, which gives the stoichiometric compound $Y_{0.80}MnO_{2.7+\delta}$. There is no excess oxygen in the yttrium deficient structure ($\delta = - 0.002$) during cooling in N_2 atmosphere, and the same observation is seen for $YMnO_3$. This is reasonable as the partial pressure of oxygen is small. In oxidizing atmosphere an oxygen adsorption of $\delta = 0.034$ is calculated for $YMnO_3$, while for $Y_{0.80}MnO_3$ a smaller adsorption of $\delta = 0.013$ was found.

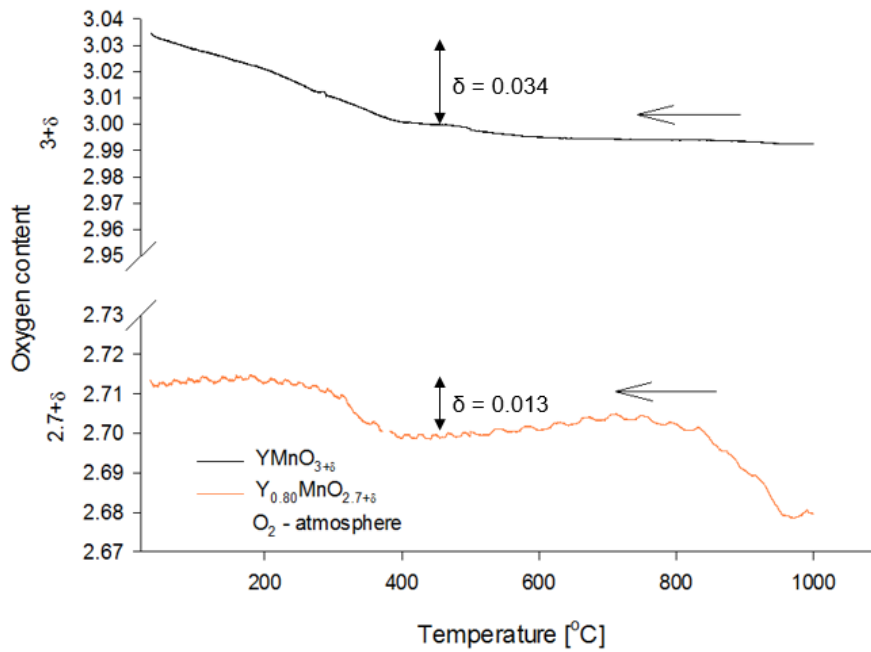


Fig. 5.3: Thermogravimetric data showing excess oxygen as a function of temperature in O_2 atmosphere for both $YMnO_{3+\delta}$ (black) and $Y_{0.80}MnO_{2.7+\delta}$ (orange). The calculated excess oxygen is $\delta = 0.034$ for $YMnO_3$ and $\delta = 0.013$ for $Y_{0.80}MnO_3$ at room temperature.

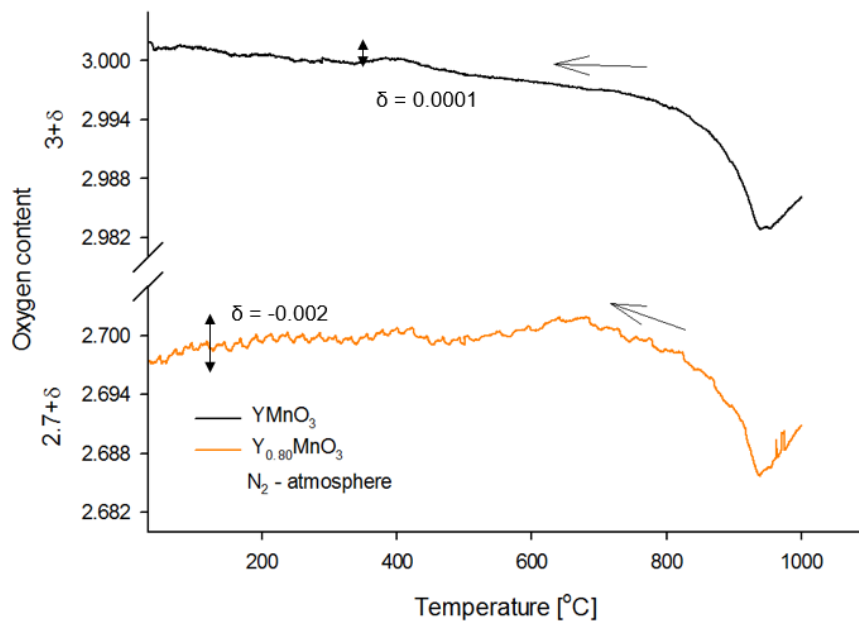
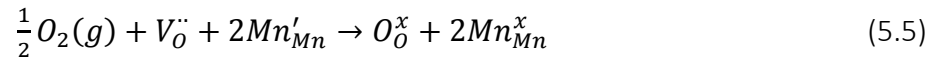
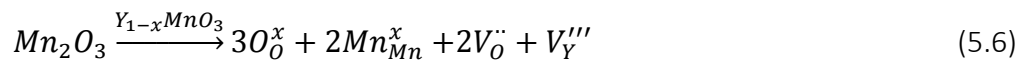


Fig. 5.4: Thermogravimetric data showing excess oxygen as a function of temperature in N_2 atmosphere for both $YMnO_{3+\delta}$ (black) and $Y_{0.80}MnO_{2.7+\delta}$ (orange). The calculated oxygen content is $\delta = 0.0001$ for $YMnO_3$ and $\delta = -0.002$ for $Y_{0.80}MnO_3$ at room temperature.

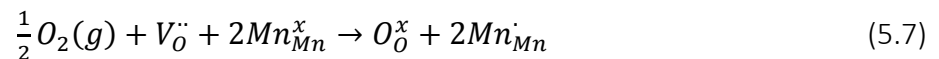
The substantial increase in oxygen content from higher temperatures to around 800 °C is believed to be attributed to filling of oxygen vacancies in both $YMnO_3$ and $Y_{0.80}MnO_3$. This is also supported by the chemical expansion seen at higher temperatures for $YMnO_3$ found by Selbach et al. [24]. The filling of oxygen vacancies during cooling from $T > 800$ °C is seen by the following Kröger-Vink notation. This is the same as equation (5.3), only in opposite direction.



From approximately 400 °C – 800 °C a stabilization of Mn^{3+} is assumed, which gives stoichiometric compounds as mentioned above. For $Y_{0.80}MnO_3$, it is here believed that one yttrium vacancy is charge compensated by two oxygen vacancies. This is shown by the following Kröger-Vink notation



When the temperature is around 400 °C the oxygen content is increasing again with decreasing temperature (besides the anomalously behavior seen for $Y_{0.80}MnO_{2.7+\delta}$ in N_2). The increasing oxygen content for $Y_{0.80}MnO_{2.7+\delta}$ in O_2 atmosphere is suggested to be filling of oxygen vacancies, with a following oxidation of Mn^{3+} to Mn^{4+} to charge compensate, shown by



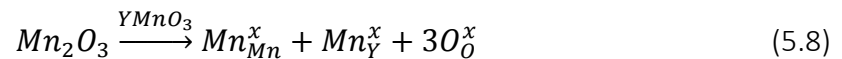
The probability of oxygen vacancies at such low temperatures is believed to be low for stoichiometric $YMnO_{3+\delta}$. The increase in oxygen content is therefore believed to be interstitial oxygen going into the structure. Even though ion mobility is low at these temperatures, can a decrease in activation energy for ion hopping make this possible. The Kröger-Vink notation for interstitial oxygen with a following oxidation of Mn^{3+} to Mn^{4+} is seen in equation (5.4), with Mn^{4+} described as Mn^{3+} with an electron-hole. According to these results, $YMnO_3$ is still believed to be a semiconducting material with p-type conductivity at low temperatures, and n-type conductivity at temperatures around 1000 °C. The same cannot be assumed for $Y_{0.80}MnO_3$, as oxygen vacancies are believed to be more dominated at lower temperatures compared to $YMnO_3$.

Chapter 5: Discussion

If yttrium deficiency in general are charge compensated by oxygen vacancies, leaving planar sites available in the Mn-plane, this may give rise to higher conductivity. As the ion conductivity is believed to be in the ab plane, a removal of oxygen will give a higher degree of available sites that O^{2-} can jump between. However, electrical conductivity measurements performed on $Y_{0.90}MnO_3$ in a preliminary master's thesis [40] gave a relatively low conductivity (same range as $YMnO_3$). This only shows that more research has to be done to get a better understanding of the defect chemistry in yttrium deficient $YMnO_3$.

The possibility of anti-sites in the hexagonal structure

Since the ionic radii of Y^{3+} (0.96 Å [32]) is not much larger than the ionic radii of Mn^{2+} (0.83 Å), there might be a possibility of anti-site between Mn and Y in the structure. The anti-site for Mn on Y site is shown for stoichiometric $YMnO_3$ by the following Kröger-Vink notation



Since Mn^{2+} forms at higher temperature, the anti-site is thus more likely to happen at higher temperatures. To investigate this probability, anti-site in $Y_{0.80}MnO_3$ was calculated in Rietveld. The anti-site gave no better fit, than without anti site. The probability is therefore suggested to be small. An empty "Y vacancy" in the middle of the trigonal bipyramidal environment would not give stabilization to the surrounding oxygen, and the structure could perhaps be destabilized. Although the suggestions is pointing towards a lower possibility for anti-site defects at lower temperature, little is known about the structure and one cannot totally decline the possibility.

5.2.4 The positions of interstitial oxygen in $YMnO_{3+\delta}$

There are several sites in the hexagonal structure that has enough space to accommodate an interstitial oxygen. Two of the most probable sites for oxygen interstitial is between three Mn atoms in the MnO_5 layers, and is represented in Figure 5.5.

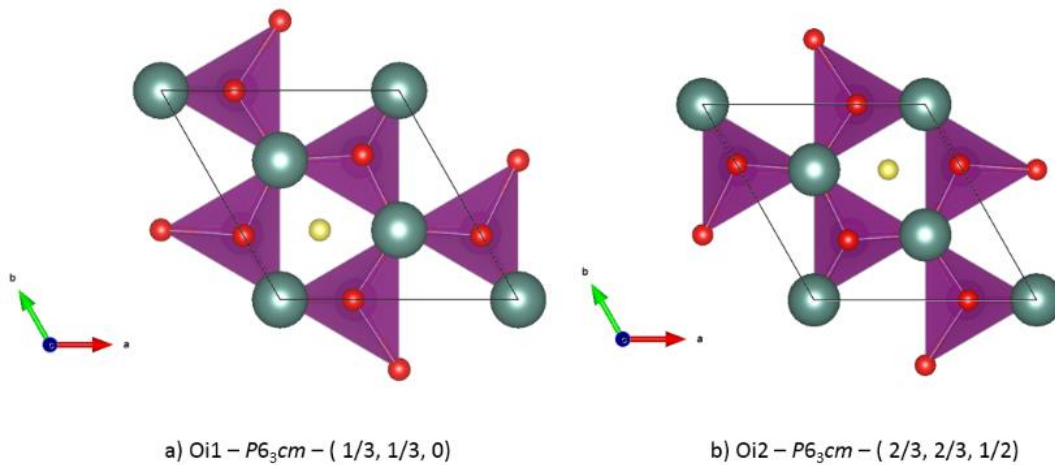


Fig. 5.5: Position of interstitial oxygen (yellow atom) in the $P6_3cm$ structure, seen from the c-axis.

The main reason for these positions of interstitial oxygen is because manganese can exhibit different oxidation states. One interstitial oxygen in the middle of three Mn atoms, will oxidize two Mn^{3+} to Mn^{4+} , while one is left as Mn^{3+} . It is believed that anti bonding bonds are formed between electrons from the O 2p orbital and the Mn d orbital. Due to electrostatics it is believed that the manganese atoms will be drawn towards the interstitial oxygen, while nearby oxygen will be repelled. It is not clear how this influence the rest of the unit cell. An interstitial oxygen will create an octahedral surrounding around manganese. The octahedral crystal field splitting for manganese in oxidation state Mn^{3+} and Mn^{4+} is viewed in Figure 5.6. The crystal field stabilization is more stable for Mn^{4+} compared to Mn^{3+} , as there is needed more energy to excite an electron up to the e_g orbitals.

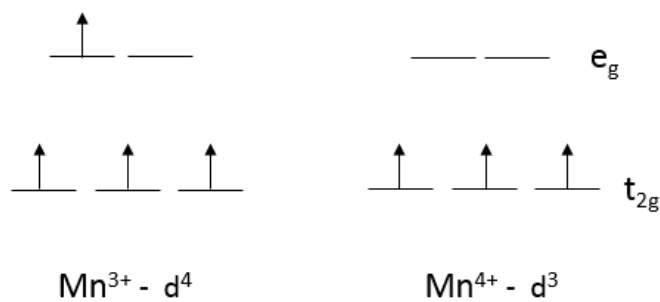


Fig. 5.6: Octahedral crystal field splitting showing Mn^{3+} and Mn^{4+} .

Chapter 5: Discussion

5.2 Structure and evaluation of the asymmetric membrane $\text{YMn}_{0.85}\text{Ti}_{0.15}\text{O}_3$

5.2.1 Decreased c/a ratio with titanium substitution in YMnO_3

15 % titanium substitution in nanocrystalline YMnO_3 resulted among others in a disappearance of the (102) and (202) super reflections, seen in Figure 4.7. The x-ray diffraction pattern for nanocrystalline $\text{YMn}_{0.85}\text{Ti}_{0.15}\text{O}_3$ was matched to the paraelectric high temperature phase which indicates a stabilization of space group $P6_3/mmc$. The phase transition was expected as it has been observed in preliminary master's thesis [[40]] and by S.Nesdal and Tomczyk.et.al[15, 39].

The disappearance of the same reflections were also expected for the x-ray diffraction patterns of the porous supports, but this was not observed. The Rietveld analysis of the porous support P2 within space group $P6_3cm$, gave unit cell parameters in almost the same ranges as the unit cell parameters for $\text{YMn}_{0.90}\text{Ti}_{0.10}\text{O}_3$ found by S.Nesdal[15], and can be seen in Table 5.1. The unit cell parameter a has a value between unit cell parameters a for $\text{YMn}_{0.90}\text{Ti}_{0.10}\text{O}_3$ and $\text{YMn}_{0.85}\text{Ti}_{0.15}\text{O}_3$, while unit cell parameter c lies somewhere between values of $\text{YMn}_{0.95}\text{Ti}_{0.05}\text{O}_3$ and $\text{YMn}_{0.90}\text{Ti}_{0.10}\text{O}_3$. It is therefore suggested that the porous supports contain less Ti, which is also supported by the non-disappearance of the Bragg reflections belonging to the (102) and (202) planes. This is a strange result as general solid state synthesis is easy to control as the amount of oxide is weighed out manually in stoichiometric amounts.

With increased titanium substitution a decrease in the c/a ratio is seen compared to pure YMnO_3 . The c/a ratio for $\text{YMn}_{0.85}\text{Ti}_{0.15}\text{O}_3$ (P2) is found to be 1.840 compared to 1.856 for YMnO_3 . This reduces the anisotropic thermal expansion in the high temperature phase transition from $P6_3/mmc$ to $P6_3cm$, which also reduce microcracking in the material. It is hard to decide from the SEM micrographs of the porous support and active layer in Figure 4.8, if microcracking in the material has been reduced.

Tab. 5.1: Unit cell parameters, unit cell volume and c/a ratio from Rietveld analysis of the porous support P2 of $\text{YMn}_{0.85}\text{Ti}_{0.15}\text{O}_2$ and bulk YMnO_3 made by solid state synthesis, within space group $P6_3cm$. To compare values, the unit cell parameters, unit cell volume and c/a ratio is shown for increased titanium substitution in YMnO_3 obtained by S.Nesdal [27], and the active layer of nanocrystalline $\text{YMn}_{0.85}\text{Ti}_{0.15}\text{O}_2$.

	R_{wp}	a [Å]	c [Å]	V [Å ³]	c/a ratio
YMnO_3	8.162	6.1398(3)	11.3990(2)	372.14(4)	1.856
$\text{YMn}_{0.85}\text{Ti}_{0.15}\text{O}_3^*$ (active layer)	18.045	6.174(7)	11.26(6)	371.99	1.888
$\text{YMn}_{0.85}\text{Ti}_{0.15}\text{O}_2$ (porous support P2)	15.876	6.1778(1)	11.367(2)	375.7(1)	1.840
$\text{YMn}_{0.95}\text{Ti}_{0.05}\text{O}_3^{**}$	3.964	6.1523	11.3767	372.92	1.849
$\text{YMn}_{0.90}\text{Ti}_{0.10}\text{O}_3^{**}$	6.166	6.1682	11.3349	373.48	1.837
$\text{YMn}_{0.85}\text{Ti}_{0.15}\text{O}_3^{**}$	6.670	6.1840	11.2758	373.19	1.823

*The active layer of $\text{YMn}_{0.85}\text{Ti}_{0.15}\text{O}_3$ converted to $P6_3cm$ basis by equation (2.1), $a_{P6_3cm} = 3^{1/2}a_{P6_3/mmc}$.

**Unit cell parameters obtained by S.Nesdal[15] within space group $P6_3cm$

A shift towards lower 2θ values of the Bragg reflections associated with the (110), (111) and (112) planes were observed for both porous supports and active layer compared to bulk YMnO_3 . For the Bragg reflection belonging to the (004) plane a shift was observed towards higher 2θ values. Increased Ti in YMnO_3 , will expand the unit cell in the basal plane, while the c-axis will be compressed. A more pronounced shift to the left is seen for nanocrystalline powder compared the porous support for the intensity belonging to the (004) plane. This is in accordance to Vegards law that unit cell parameters will scale with the chemical composition. The increase of the unit cell length a, together with a compression along the c-axis is then attributed to a reduced tilting of the MnO_5 and less displacement of the yttrium atoms.

Structure analysis consideration of the active layer consisting of nanocrystalline $\text{YMn}_{0.85}\text{MnO}_3$ prepared by citric acid method

When dealing with Rietveld analysis of nanocrystalline powder it is important to have a tight distribution of crystallite size in the powders, as a wide distribution can cause nonrandomness. Today, it is not possible to correct for nonrandomness in Topas. Line broadening will also be an issue for nanocrystalline powders as seen in Fig. 4.7. This gives uncertainties in the calculation of crystallite size, and is probably the reason for the few nm higher value than expected for the crystallite size compared to the results from Bergum.et.al found at 800° C. For a better indication of the distribution and correct crystallite size, TEM micrographs should be used. It should also be noted that the fundamental parameters for the D8 focus are still not perfects and correction for instrumental errors could be slightly inaccurate.

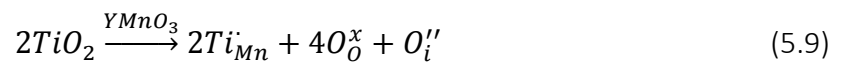
Besides the high broadening of the peaks seen in the XRD path of nanocrystalline $\text{YMn}_{0.85}\text{Ti}_{0.15}\text{O}_3$, everything coincide with a phase transition from the low temperature phase to the high temperature phase. Although Bergum et.al [17] found an increase in the unit cell length a, and a decrease in unit cell parameter c, which gave a decrease in unit cell volume with

Chapter 5: Discussion

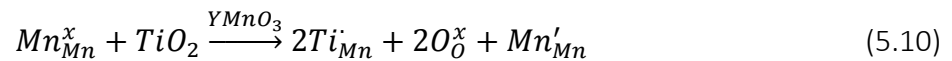
decreasing crystallite size, there is not seen any abnormal results of the nanocrystalline $YMn_{0.85}Ti_{0.15}O_3$. There is a possibility that decreased crystallite size give a higher symmetry structure because of the increased randomness caused by a loss of coherence in the structure.

5.2.2 Oxygen non-stoichiometry with titanium substitution in $YMnO_3$

It is suggested that titanium substitution will stabilize excess oxygen in the material. The proposed mechanism for this is that Ti^{4+} stabilize O^{2-} by the formula $YMn_{1-x}Ti_xO_{3+(x/2)}$, where $x/2$ is the same as δ . For $x = 10$, this value becomes $\delta = 0.05$, that almost corresponds to the value obtained by TGA, $\delta=0.043$, found by S.Nesdal[15]. The stabilization of excess oxygen or in other words stabilization of interstitial oxygen is described by the following Kröger-Vink notation,



This may explain the high electronic conductivity at 400 ° C found for $YMn_{0.85}Ti_{0.15}O_3$ compared to $YMnO_3$ in the preliminary master's thesis [40], as there is created more charge carrier holes. However, Ti^{4+} has zero electrons in the d-orbital and one would expect a lower electronic mobility. Another assumption is that Ti^{4+} is charge compensated by reduction of Mn^{3+} to Mn^{2+} , seen as follows



This will change manganese from $3d^4$ to $3d^5$, and one electron has to go up in the fairly localized d_{z^2} orbital as shown in Figure. 5.7. This excitation required more energy than the other oxidation states of Mn within the trigonal bipyramidal crystal field splitting.

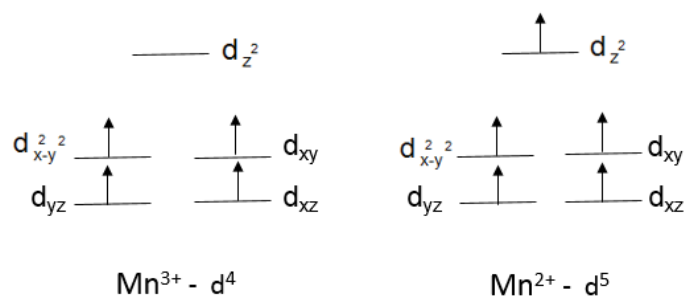


Fig. 5.7: Trigonal bipyramidal crystal field splitting showing Mn^{3+} and Mn^{2+} .

5.2.3 Evaluation of the active layer and the porous supports after sintering.

Even though the synthesis of nanocrystalline powder was successful, a dense ceramic membrane was not obtained after sintering, as seen in Figure 4.8. There can be several reasons for this. One reason can be due to agglomerates in the powder that hinders close packing (smaller distance between particles) of the powder before sintering. Powder that is not sufficient close packed gives has a high diffusion distance which gives limited densification during sintering. The density of particles solved in ethanol could also have been too high, which also gives a relatively poor close packed powder upon the porous support. This can also be the reason for why the double and triple dip coated membranes had almost the same thickness of the active layer, seen in Figure 4.9. To solve problems with close enough packing of powder on top of the porous support surfactant and/or ball milling can be used. After crystallization of the nanocrystalline powder a following ball milling could decrease the particle size. This powder could be used in a dispersion containing ethanol and surfactants to prevent agglomeration. The dispersion stability can have a significant effect on the performance, resulting in poor adhesion, insufficient reactivity and film thickness. There are however no reports on how to make a stable dispersion using surfactants and hexagonal YMnO_3 .

The prospect of using titanium substitution in YMnO_3 as membrane material has a great advantage as the electrical conductivity is higher for titanium doped YMnO_3 compared to YMnO_3 . Furthermore, a decrease in the c/a ratio have proven to give reduced microcracking which is a great advantage in processing membranes. In addition, a suggestion of ionic conductivity at lower temperatures due to interstitial oxygen is a great advantage with regards of reducing the operational temperatures for MIEC membranes. However, more attention has to be given to the defect chemistry in YMnO_3 , and a more systematic synthesis procedure has to be found in order to obtain a dense and functional layer on top of a porous support. The two components of the membrane also have to be in the same structural composition to avoid thermal and chemical expansion problems which will lead to cracks or degradation of the membrane. In this thesis, the same structure was not obtained for both the porous support and active layer due to artificial wrongs.

5.5 Further work

The limiting understanding of point defects in hexagonal manganites, must be further investigated. Thermogravimetric analysis in both oxidizing and reducing atmospheres on 10 % and up to 30 % yttrium deficiency in YMnO_3 can give an indication of how the excess oxygen varies for different amount of yttrium in the structure. Dilatometry on yttrium deficient samples will also give an indication of how yttrium deficiency in YMnO_3 influence the phase transition between the low and high temperature phase. The understanding of defect chemistry in hexagonal manganites are important as the concentration of defects can tune different properties of the material. Thus for instance optimize the electrical conductivity in YMnO_3 . The positions of interstitial oxygen and oxygen vacancies are crucial in the understanding of how defects in YMnO_3 influence the structure. These positions should be investigated by DFT calculations, to find out which position gives the lowest energy. The next stage when it comes to processing a MIEC membrane is to find a synthesis method that gives a dense and functional

Chapter 5: Discussion

layer on top of a porous support. Addition of surfactants in a slurry with nanocrystalline powder and ethanol will prevent agglomeration and give a denser packed layer before sintering. The performance (oxygen permeation rate) of such a membrane will give a good indication of how the membrane will work in practice and how the properties influence the stability.

7. Conclusion

This work was performed to investigate how the structure and oxygen storage ability changes with different yttrium content in YMnO_3 . Hexagonal YMnO_3 has the ability to lose 15-20 % yttrium without any notable changes in the structure and composition for yttrium deficient YMnO_3 . Above this limit, reflections from Mn_3O_4 hausmannite appears in x-ray diffractograms. The same solubility limit was also found for yttrium deficient samples of YMnO_3 heated in N_2 and O_2 atmospheres. With a higher degree of yttrium deficiency in the hexagonal structure prepared in air, a slight contraction of the unit cell along both the a and c axis is found. For yttrium deficient samples annealed in oxidizing (O_2) atmosphere, the structure expands in the along the a axis and contracts along the c-axis. The opposite behavior is seen in reducing (N_2) atmosphere, where the structure expands in c direction and contract along the a axis with increased yttrium deficiency in YMnO_3 . Above 600 °C, during heating of YMnO_3 and $\text{Y}_{0.80}\text{MnO}_3$, oxygen goes out of the materials in both N_2 and O_2 atmospheres. Upon cooling in O_2 atmosphere, a reversible oxygen uptake is seen around 400 °C for both YMnO_3 and yttrium deficient YMnO_3 . For stoichiometric YMnO_3 the reversible oxygen adsorption is suggested to be attributed to interstitial oxygen, while for stoichiometric yttrium deficient YMnO_3 there is believed to be filling of oxygen vacancies. The asymmetric membrane of $\text{YMn}_{0.85}\text{Ti}_{0.15}\text{O}_3$ did not yield a dense functional layer on top of the porous support after sintering, and the membrane thickness was the same after double and triple dip coatings. The results from this thesis highlights the huge possibilities hexagonal manganites have for use in MIEC membranes. More attention has to be given to hexagonal manganites to get a better understanding of the properties, and to get one step further to a more environmentally friendly world.

Bibliography

1. Armaroli, N. and V. Balzani, *The future of energy supply: challenges and opportunities*. Angewandte Chemie International Edition, 2007. **46**(1-2): p. 52-66.
2. Bouwmeester, H., H. Kruidhof, and A. Burggraaf, *Importance of the surface exchange kinetics as rate limiting step in oxygen permeation through mixed-conducting oxides*. Solid State Ionics, 1994. **72**: p. 185-194.
3. Bouwmeester, H.J., *Dense ceramic membranes for methane conversion*. Catalysis Today, 2003. **82**(1): p. 141-150.
4. Hendriksen, P.V., et al., *Prospects and problems of dense oxygen permeable membranes*. Catalysis Today, 2000. **56**(1): p. 283-295.
5. Hashim, S.M., A.R. Mohamed, and S. Bhatia, *Current status of ceramic-based membranes for oxygen separation from air*. Advances in colloid and interface science, 2010. **160**(1): p. 88-100.
6. Leo, A., S. Liu, and J.C. Costa, *Development of mixed conducting membranes for clean coal energy delivery*. International Journal of Greenhouse Gas Control, 2009. **3**(4): p. 357-367.
7. Bartonickova, E., et al., *Synthesis and oxygen transport properties of $\text{La}_{0.2}\text{Sr}_{0.8}\text{Fe}_{1-x}\text{Ti}_x\text{O}_{3-\delta}$* (x). Journal of the European Ceramic Society, 2010. **30**(2): p. 605-611.
8. Lemes-Rachadel, P., et al., *Current developments of mixed conducting membranes on porous substrates*. Materials Research, 2013(AHEAD): p. 0-0.
9. (CO2CRC), C.f.G.G.T., et al. *Callide Oxyfuel Project*. 2013 [cited 2013 01.12.2013]; Web page]. Available from: <http://www.callideoxyfuel.com/>.
10. Sunarso, J., et al., *Mixed ionic–electronic conducting (MIEC) ceramic-based membranes for oxygen separation*. Journal of Membrane Science, 2008. **320**(1): p. 13-41.
11. Chen, C., et al., *Oxygen permeation of $\text{La}_{0.3}\text{Sr}_{0.7}\text{CoO}_{3-\delta}$* . Solid State Ionics, 1997. **98**(1): p. 7-13.
12. Lein, H.L., *Mechanical Properties and Phase Stability of Oxygen Permeable Membranes $\text{La}_{0.5}\text{Sr}_{0.5}\text{Fe}_{1-x}\text{Co}_x\text{O}_{3-\delta}$* . 2005, Norwegian University of Science and Technology.
13. Kaus, I., et al., *Oxygen transport properties in $\text{La}_{1-x}\text{Sr}_x\text{Fe}_{1-y}\text{M}_y\text{O}_{3-\delta}$ (M= Cr, Ti), 0.2 bx 0. 8, 0.2 byTi b0. 5, 0.1 byCr b0. 3*. Solid State Ionics, 2007. **178**: p. 817-826.
14. Remsen, S. and B. Dabrowski, *Synthesis and Oxygen Storage Capacities of Hexagonal $\text{Dy}_{1-x}\text{Y}_x\text{MnO}_{3+\delta}$* . Chemistry of Materials, 2011. **23**(17): p. 3818-3827.
15. Nesdal, S.K., *Development of hexagonal manganites for use in oxygen permeable membranes*, in *Materials Science and Engineering*. 2013, NTNU: NTNU.
16. Tilley, R.J., *Understanding solids: the science of materials*. 2004: John Wiley & Sons.
17. Bergum, K., et al., *Synthesis, structure and magnetic properties of nanocrystalline YMnO_3* . Dalton Transactions, 2011. **40**(29): p. 7583-7589.
18. Dubourdieu, C., et al., *Thin films and superlattices of multiferroic hexagonal rare earth manganites*. Philosophical Magazine Letters, 2007. **87**(3-4): p. 203-210.
19. Yoo, Y., et al., *Spin-glass behavior of Cr-doped YMnO_3 compounds*. Journal of Applied Physics, 2012. **112**(1): p. 013903.

20. Yang, L., et al., *Ferrimagnetism and possible double perovskite structure in half Cr-doped $YMn_{0.5}Cr_{0.5}O_3$* . Journal of Alloys and Compounds, 2013. **570**: p. 41-45.
21. Degenhardt, C., et al., *Nonlinear optical spectroscopy of electronic transitions in hexagonal manganites*. Applied Physics B, 2001. **73**(2): p. 139-144.
22. Jiang, N. and X. Zhang, *Atomistic simulation of Mn-site substitution in multiferroic $h-YMnO_3$* . Journal of Physics: Condensed Matter, 2012. **24**(23): p. 235402.
23. Gelard, I., et al., *Off-stoichiometry effects on the crystalline and defect structure of hexagonal manganite $REMnO_3$ films ($RE = Y, Er, Dy$)*. Chemistry of Materials, 2011. **23**(5): p. 1232-1238.
24. Selbach, S.M., et al., *Crystal structure, chemical expansion and phase stability of $HoMnO_3$ at high temperature*. Journal of Solid State Chemistry, 2012. **196**: p. 528-535.
25. Kumagai, Y., et al., *Observation of persistent centrosymmetry in the hexagonal manganite family*. Physical Review B, 2012. **85**(17): p. 174422.
26. Momma, K. and F. Izumi, *VESTA: a three-dimensional visualization system for electronic and structural analysis*. Journal of Applied Crystallography, 2008. **41**(3): p. 653-658.
27. Gibbs, A.S., K.S. Knight, and P. Lightfoot, *High-temperature phase transitions of hexagonal $YMnO_3$* . Physical Review B, 2011. **83**(9): p. 094111.
28. Aken, B.v., A. Meetsma, and T.T. Palstra, *Hexagonal $YMnO_3$* . Acta Crystallographica Section C: Crystal Structure Communications, 2001. **57**(3): p. 230-232.
29. Singh, K., et al., *Analysis of the multiferroicity in the hexagonal manganite $YMnO_3$* . Journal of Physics: Condensed Matter, 2013. **25**(41): p. 416002.
30. Yokokawa, H., et al., *Thermodynamic stabilities of perovskite oxides for electrodes and other electrochemical materials*. Solid State Ionics, 1992. **52**(1): p. 43-56.
31. Goldschmidt, V.M., *Die gesetze der krystallochemie*. Naturwissenschaften, 1926. **14**(21): p. 477-485.
32. Shannon, R., *Revised effective ionic radii and systematic studies of interatomic distances in halides and chalcogenides*. Acta Crystallographica Section A: Crystal Physics, Diffraction, Theoretical and General Crystallography, 1976. **32**(5): p. 751-767.
33. Remsen, S., et al., *Synthesis and oxygen content dependent properties of hexagonal $DyMnO_{3+\delta}$* . Journal of Solid State Chemistry, 2011. **184**(8): p. 2306-2314.
34. Chen, M., B. Hallstedt, and L.J. Gauckler, *Thermodynamic assessment of the Mn-Y-O system*. Journal of Alloys and Compounds, 2005. **393**(1-2): p. 114-121.
35. Smith, A.E., et al., *Mn^{3+} in trigonal bipyramidal coordination: a new blue chromophore*. Journal of the American Chemical Society, 2009. **131**(47): p. 17084-17086.
36. Tomczyk, M., et al., *Origin of microcracking in $YMnO_3$ ceramics*. Scripta Materialia, 2012. **66**(5): p. 288-291.
37. Nénert, G., et al., *Experimental evidence for an intermediate phase in the multiferroic $YMnO_3$* . Journal of Physics: Condensed Matter, 2007. **19**(46): p. 466212.
38. Green, D.J., *An introduction to the mechanical properties of ceramics*. 1998: Cambridge University Press.
39. Tomczyk, M., et al., *Reduction of microcracking in $YMnO_3$ ceramics by Ti substitution*. Scripta Materialia, 2012. **67**(5): p. 427-430.

40. Student: Madelen Mørk Frydenlund, S.S.M.S., *Electronic conductivity in hexagonal manganites* in *Material 2013*, Norwegian University of Science and Technology NTNU. p. 59.
41. Asaka, T., et al., *Crystallographic superstructure of Ti-doped hexagonal YMnO₃*. *Physical Review B*, 2005. **71**(1): p. 014114.
42. Lescano, G., et al., *Synthesis and electrical conductivity of Y_{1-x}Mn_{1-y}O_{3-δ}*. *Journal of the European Ceramic Society*, 2001. **21**(10): p. 2037-2040.
43. Overton, A.J., et al., *Influence of topotactic reduction on the structure and magnetism of the multiferroic YMnO₃*. *Chemistry of Materials*, 2009. **21**(20): p. 4940-4948.
44. Moure, C., et al., *Phase transition and electrical conductivity in the system YMnO₃-CaMnO₃*. *Journal of materials science*, 1999. **34**(11): p. 2565-2568.
45. Sekhar, M.C. and N.V. Prasad, *Dielectric, impedance, magnetic and magnetoelectric measurements on YMnO₃*. *Ferroelectrics*, 2006. **345**: p. 45-57.
46. Elliott, S.R. and G. Landrum, *The physics and chemistry of solids*. Vol. 62. 1998: Wiley New York.
47. Selbach, M.M.F.S.S.M., *Electronic conductivity in hexagonal manganites*, in *IMT. 2013*, NTNU: Trondheim.
48. Coble, R.L., *Sintering crystalline solids. I. Intermediate and final state diffusion models*. *Journal of Applied Physics*, 2004. **32**(5): p. 787-792.
49. Richerson, D.W., *Modern ceramic engineering: properties, processing, and use in design*. 2006, Boca Raton, Fla.: CRC Press. 707 s. : ill.
50. Katsufuji, T., et al., *Crystal structure and magnetic properties of hexagonal R MnO₃ (R= Y, Lu, and Sc) and the effect of doping*. *Physical Review B*, 2002. **66**(13): p. 134434.

Appendix A: Structural parameters with titanium substitution in YMnO_3 within space group $P6_3cm$

The structural parameters of $\text{YMn}_{1-x}\text{Ti}_x\text{O}_3$ for $x = 0.05, 0.10$ and 0.15 obtained by S.Nesdal[15] are found in Table A1. The structural parameters were refined within space group $P6_3cm$. A supporting illustration of the structural position is seen for the hexagonal space group $P6_3cm$ in Figure A1. In the same figure, a presentation of the tilting of MnO_5 bipyramids and displacement of yttrium ions associated with the low temperature phase is shown.

Tab. A1: Refined atomic positions, lattice parameters and unit cell volume with increased Ti substitution in hexagonal YMnO_3 within space group $P6_3cm$ obtained by S.Nesdal [15].

	$\text{YMn}_{0.95}\text{Ti}_{0.05}\text{O}_3$	$\text{YMn}_{0.90}\text{Ti}_{0.10}\text{O}_3$	$\text{YMn}_{0.85}\text{Ti}_{0.15}\text{O}_3$
a [Å]	6.1523	6.1682	6.1840
c [Å]	11.3767	11.3349	11.2758
V [Å ³]	372.92	373.48	373.19
R _{wp}	3.964	6.166	6.670
Y1 z	0.27414	0.25988	0.25483
Y2 z	0.23503	0.23163	0.23177
Mn x	0.34165	0.33133	0.33439
O1 x	0.27914	0.30613	0.29230
O1 z	0.16302	0.17352	0.17154
O2 x	0.66712	0.64043	0.66241
O2 z	0.33912	0.35926	0.36577
O3 z	0.49023	0.49737	0.51933
O4 z	0.02957	0.03067	0.02325

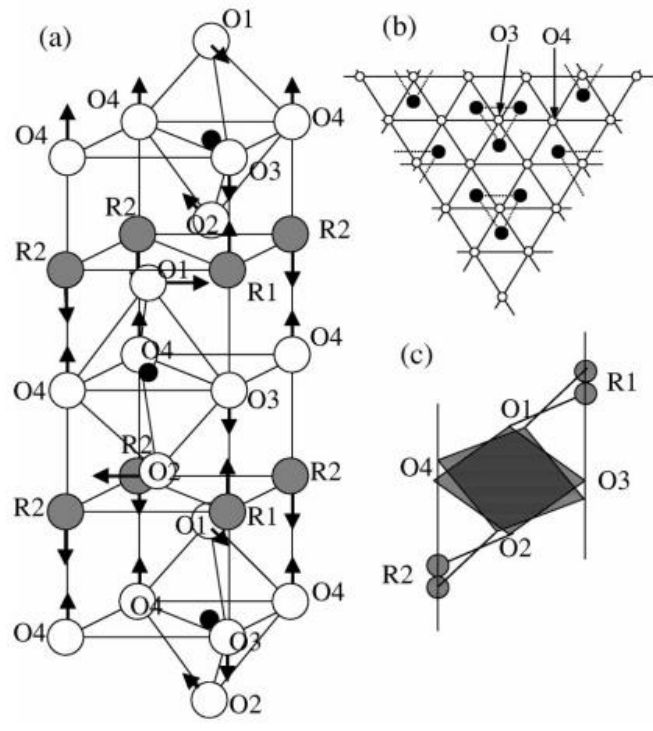


Fig. A1: A schematic representation of the atom positions showing the displacements of Y ions and tilting of MnO₅ bipyramids within space group *P6₃cm* in hexagonal YMnO₃. Figure is reprinted from Katsufuji et.al [50].

Appendix B: Preparation of Y^{3+} and Mn^{3+} precursors for the citric acid method and gravimetrically determination of the precursors molality.

Preparation of Y^{3+} precursor

The yttrium precursor was made by adding $Y(O_2C_2H_3)_3 \times H_2O$ (0.05 mole) to a 1 L conical flask together with citric acid (CA) to a molar ratio of 1:15. Short after, 1 L of distilled water was added to the conical flask. The solution was placed on a hot plate holding a temperature of 150 °C, and continuously stirred (480 rpm) with a magnet. After 17 hours (overnight), all powders were dissolved and the solution was completely blank.

Preparation of Mn^{3+} precursor

The manganese precursor was prepared by adding $Mn(CO_3) \times H_2O$ (0.05 mole) in a conical flask together with CA to a molar ratio of 1:22. The conical flask was short after added 1 L of distilled water. The same procedure for temperature and stirring was followed for the Mn^{3+} precursor as for the Y^{3+} precursor. The yellow solution became clear after about 17 hours.

Standardization of precursors

The molality of all solutions has been determined gravimetrically by heating four parallels of porcelain bowls each containing 2 ml of solution. A list of the two precursors prepared in this synthesis, their molality, their annealing temperature as well as the relative amount of citric acid to the cations is given in Table B1. Prior to heating, the porcelain bowls with lao wool lid, were heated at 1000 °C for 1 hour to avoid contamination and measurement wrongs. Figure B1 gives the temperature program for the precursors. The final products were Y_2O_3 and Mn_2O_3 , as can be seen in the XRD diffractograms in Figure B2.

Tab. B1: A list over the content in the precursors, their molality as well as their annealing temperature, made for the citric acid synthesis route.

Precursor	Weight of cation starting material [g]	Citric acid [g]	Relative amount [CA/ cations]	Molality [mmol/g]	Annealing temperature [°C]
Y^{3+}	13.302	144.09	15	0.04369	1150
Mn^{3+}	5.7475	211.33	22	0.04308	700

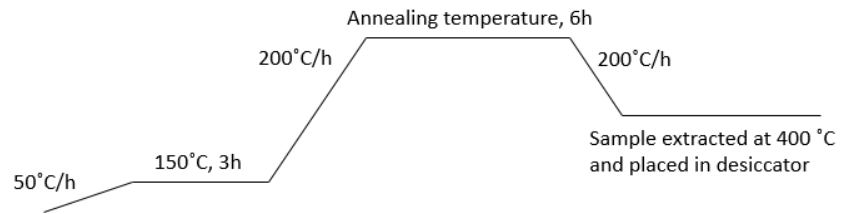


Fig.B1: Temperature program used in determining the molality of the precursors gravimetrically.

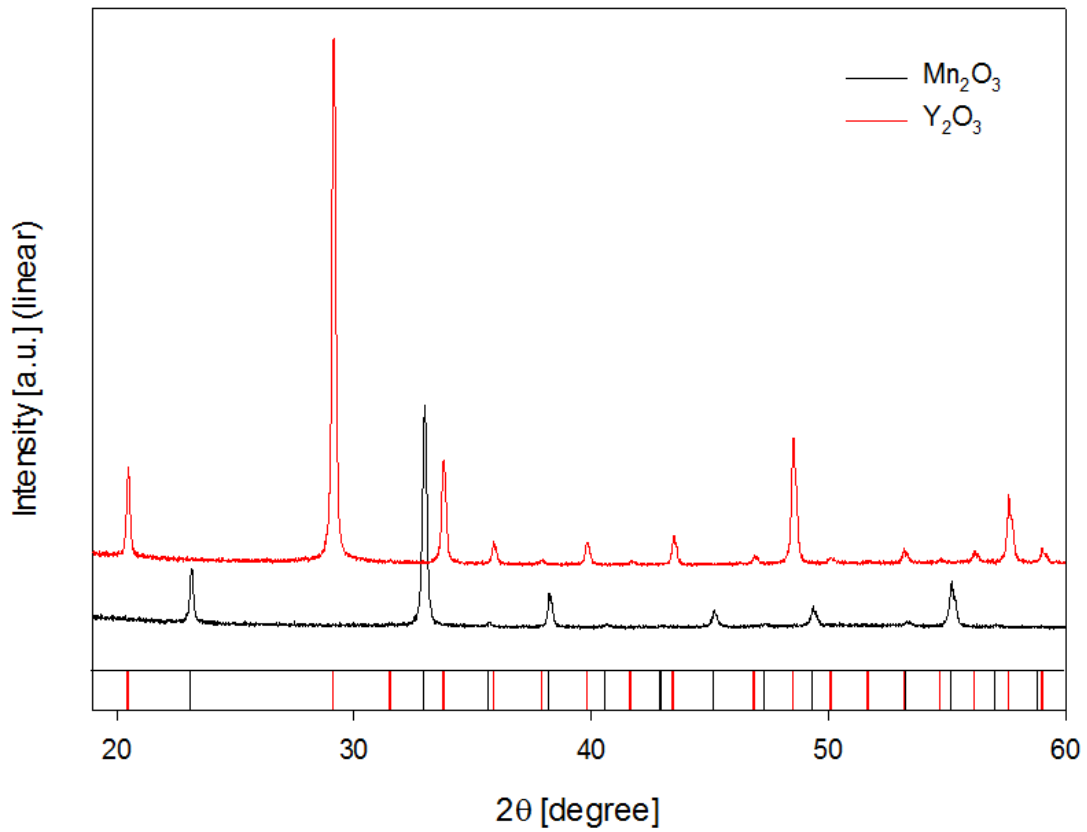


Fig. B2: XRD diffractograms of Mn₂O₃ (black) and Y₂O₃. These oxides were formed when gravimetrically deciding the molality of the precursors used for the citric acid method. The vertical lines represents the matching PFD card (00-041-1442) for Mn₂O₃ (black), and PDF card (00-043-1036) for Y₂O₃ (red)

Appendix C: X-ray diffraction pattern of pure phase YMnO_3 and porous support P1 made from solid state synthesis.

The x-ray diffractogram of phase pure YMnO_3 within space group $P6_3cm$. The matching PDF card was 04-011-9577, as is shown as dotted red lines in Figure C1. The x-ray pattern for porous support P1 of $\text{YMn}_{0.85}\text{Ti}_{0.15}\text{O}_3$ is seen in Figure C2. A posteriori displacement correction of the data, reveals a displacement of the (004) reflection towards higher 2θ values, while the reflections from the (110), (111) and (112) planes are still displaced towards lower 2θ values.

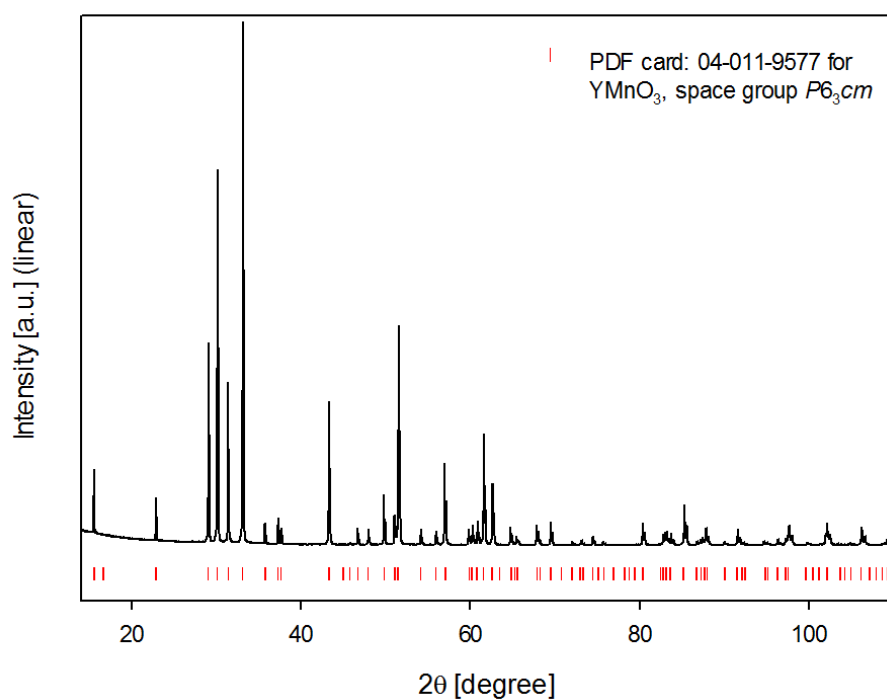


Fig. D1: X-ray diffractogram of phase pure YMnO_3 prepared by solid state synthesis within space group $P6_3cm$. The x-ray path was matched to the PDF card: 04-011-9577 belongs to hexagonal YMnO_3 and can be seen as the dotted red lines in the figure.

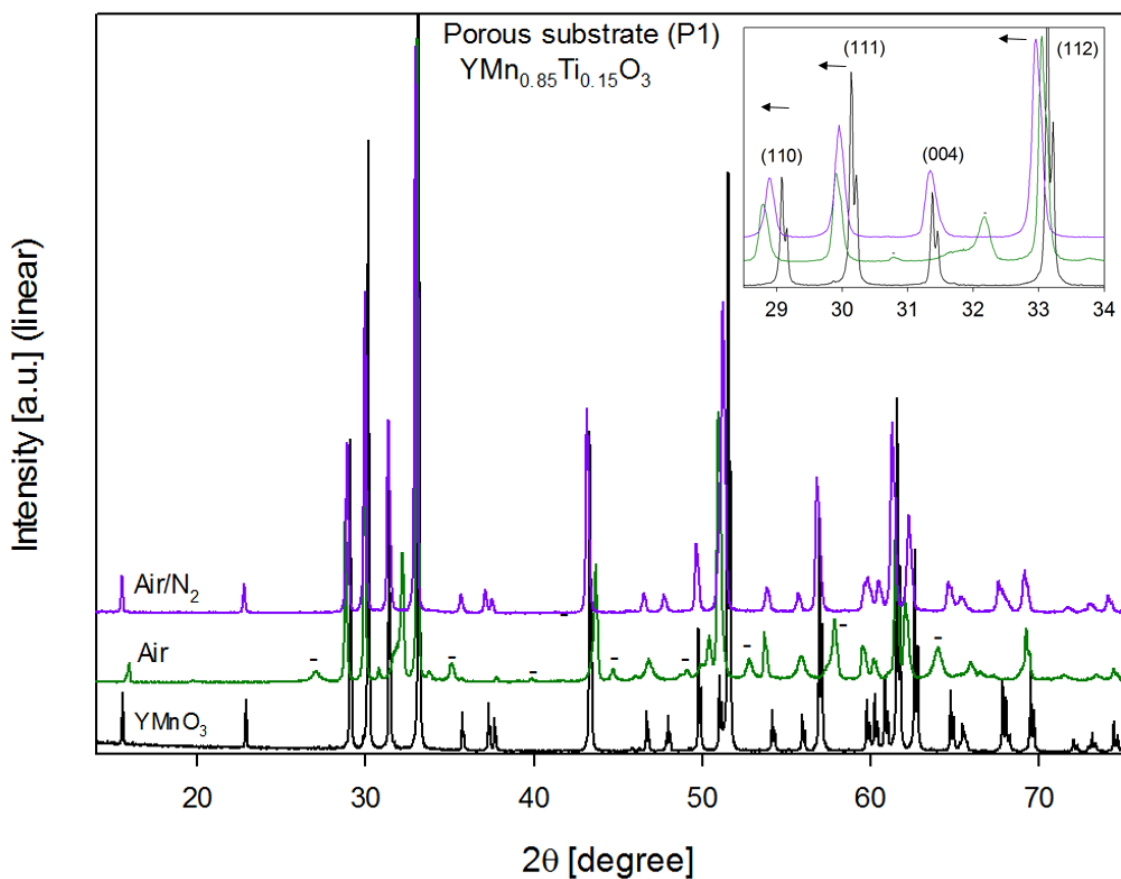


Fig. C2: X-ray diffractograms of the porous support (P1) of $\text{YMn}_{0.85}\text{Ti}_{0.15}\text{O}_3$ made by solid state synthesis that first was heated in air (green), before it was heated in N_2 (purple). The (-) indicates a secondary phase of Y_2O_3 . The x-ray diffractograms is compared to pure YMnO_3 within space group $P6_3cm$ from general solid state sintering. An excerpt of the (110), (111), (004) and (112) reflections with a smaller range of 2θ values is inserted in the top-right corner of the figure to give a better view of the displacements with titanium substitution in YMnO_3 compared to pure YMnO_3 . A posteriori displacement correction of the data, reveals a displacement of the (004) reflection towards higher 2θ values, while the reflections from the (110), (111) and (112) planes are still displaced towards lower 2θ values.

Appendix D: Rietveld refinement of YMnO_3 and $\text{YMn}_{0.85}\text{Ti}_{0.15}\text{O}_3$ (porous support P2) prepared by solid state synthesis, and nanocrystalline $\text{YMn}_{0.85}\text{Ti}_{0.15}\text{O}_3$ made by citric acid method.

The Rietveld refinement of YMnO_3 prepared by solid state synthesis within space group $P6_3cm$ is seen in Figure D1. In Figure D2 and D3, the Rietveld refinements of the porous support P2 ($\text{YMn}_{0.85}\text{Ti}_{0.15}\text{O}_3$) and nanocrystalline powder of $\text{YMn}_{0.85}\text{Ti}_{0.15}\text{O}_3$ are seen respectively. The porous support made by solid state synthesis was refined within space group $P6_3cm$, while nanocrystalline $\text{YMn}_{0.85}\text{Ti}_{0.15}\text{O}_3$ made by citric acid method is refined within space group $P6_3/mmc$.

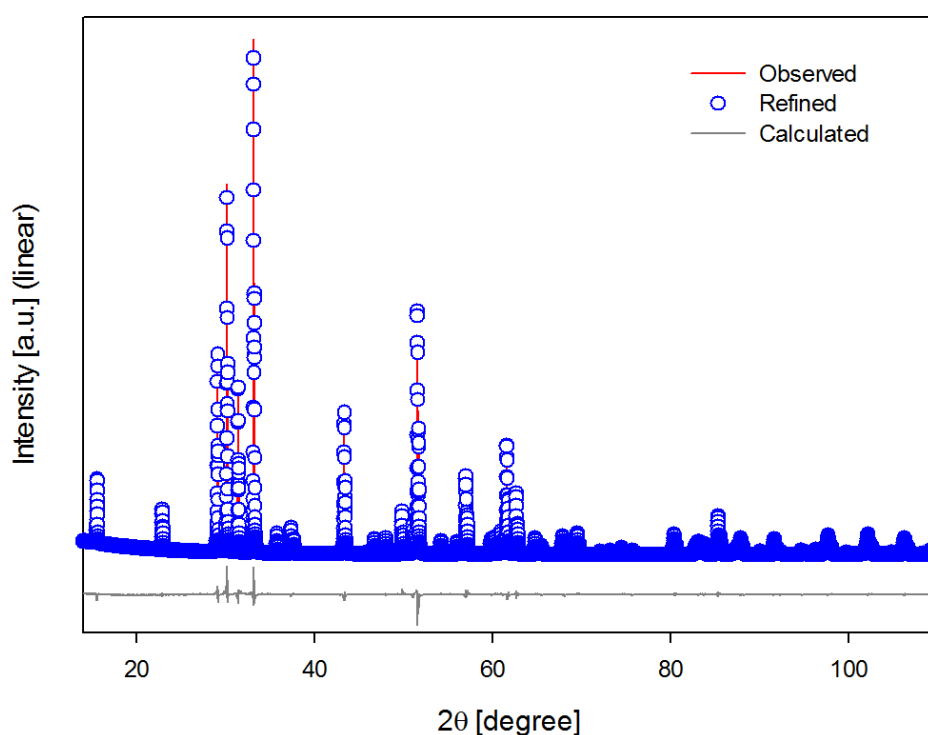


Fig. D1: Rietveld refinement of the x-ray pattern for YMnO_3 made from solid state synthesis within space group $P6_3cm$.

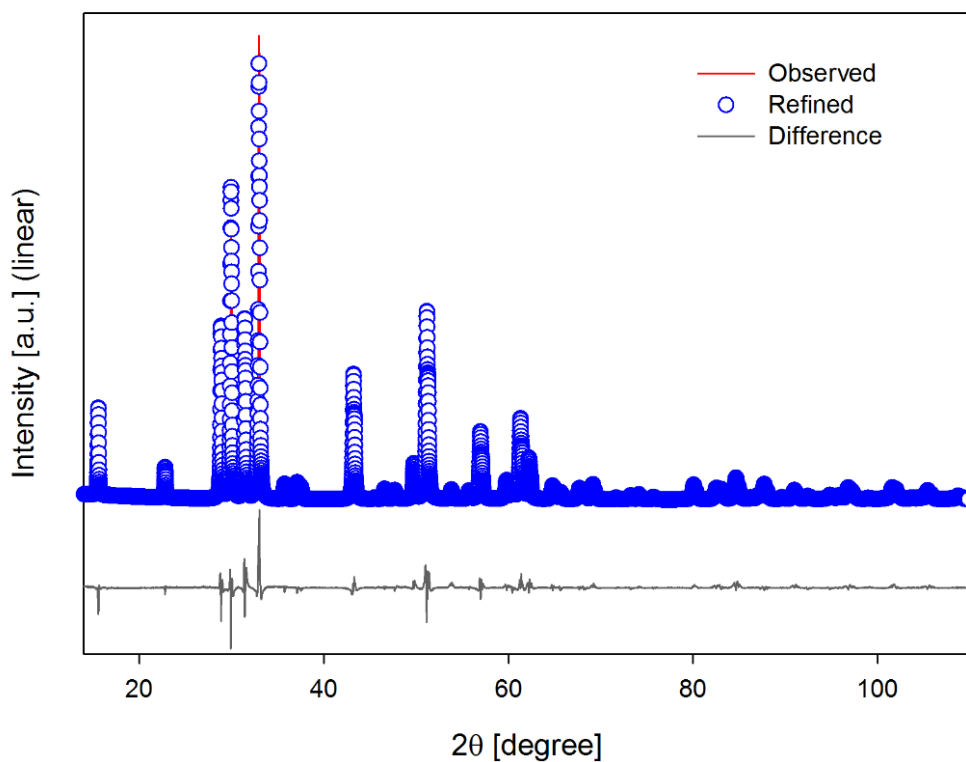


Fig. D2: Rietveld refinement of the x-ray pattern for the porous support P2 of $\text{YMn}_{0.85}\text{Ti}_{0.15}\text{O}_3$ made from solid state synthesis within space group $P6_3cm$.

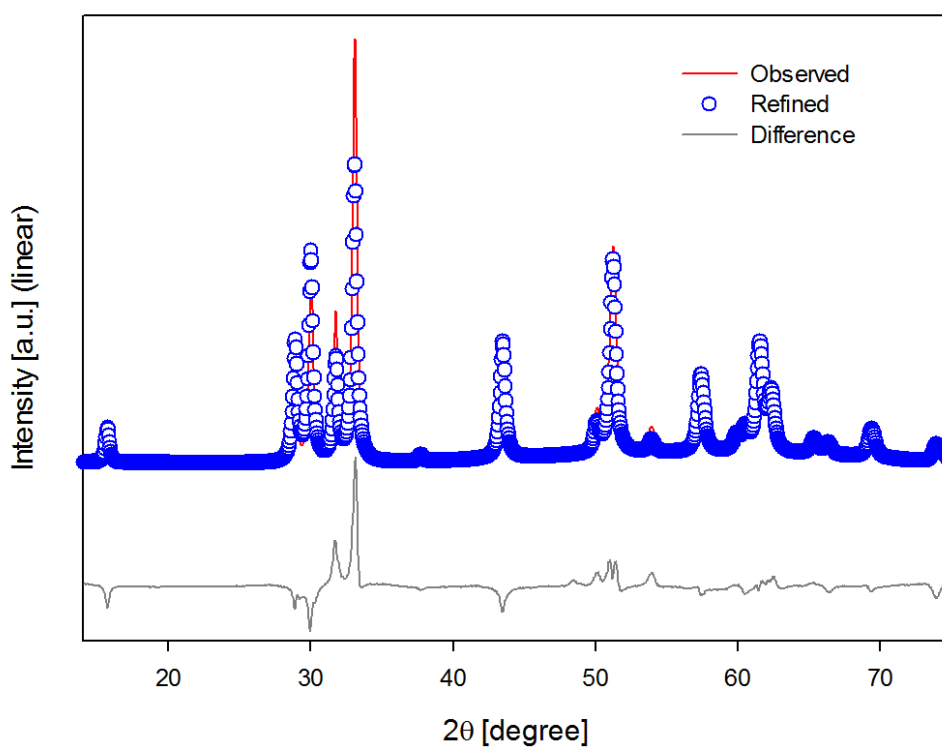


Fig D3: Rietveld refinement of x-ray pattern from nanocrystalline $\text{YMn}_{0.85}\text{Ti}_{0.15}\text{O}_3$ made by citric acid method within space group $P6_3/mmc$.

Appendix E: X-ray diffractograms of yttrium deficient YMnO_3 samples annealed in N_2 and O_2 atmospheres

X-ray diffractograms of yttrium deficient samples of YMnO_3 heated in N_2 atmosphere, seen in Figure E1, and O_2 atmosphere seen in Figure E2.

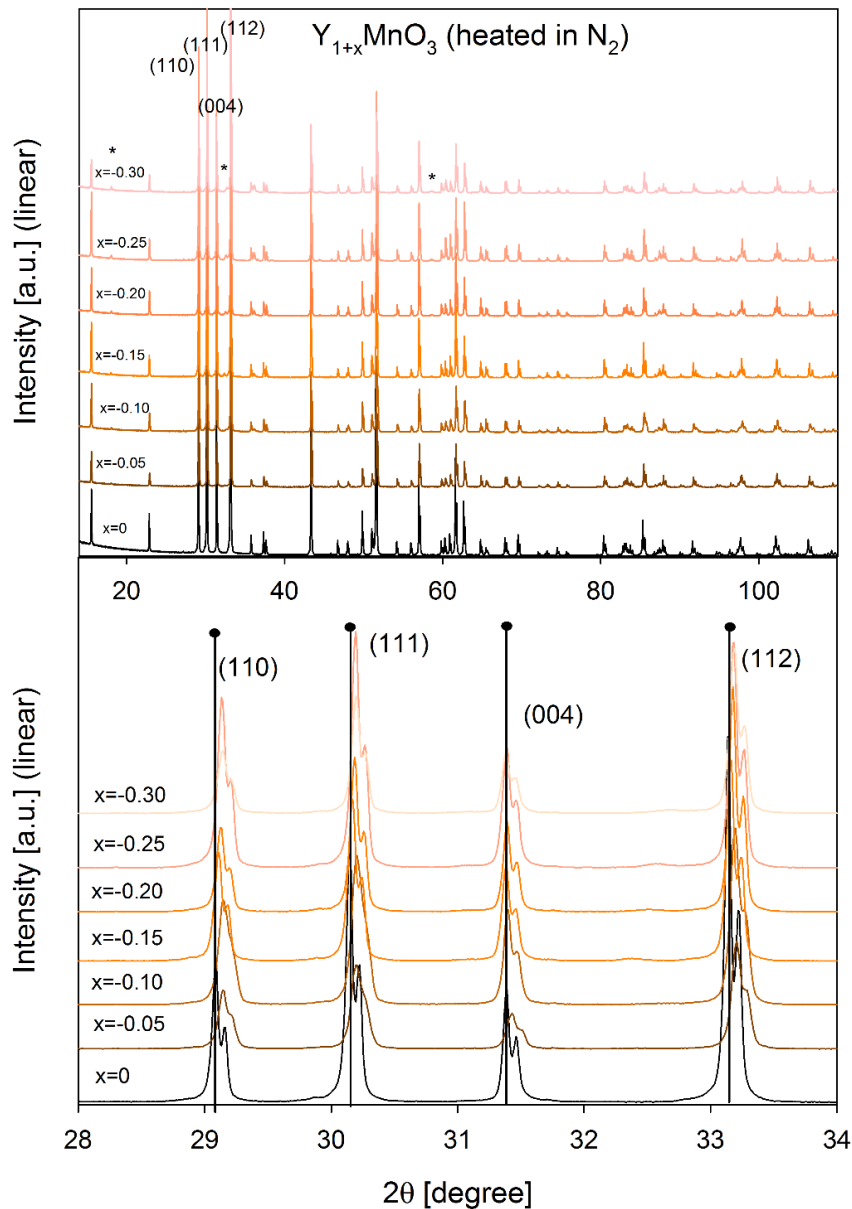


Fig. E1: X-ray diffractograms of YMnO_3 samples with varying yttrium deficiency as prepared by solid state synthesis and heated in N_2 atmosphere. The lower end of the diagram gives a better overview of the shift towards higher 2θ values for the reflections belonging to the (110), (111) and (112) planes. The vertical black lines in the lower end of the diagram is a guide to the eye to see the shift of intensities better. * is indicating the pronounced intensities of Mn_3O_4 (hausmannite).

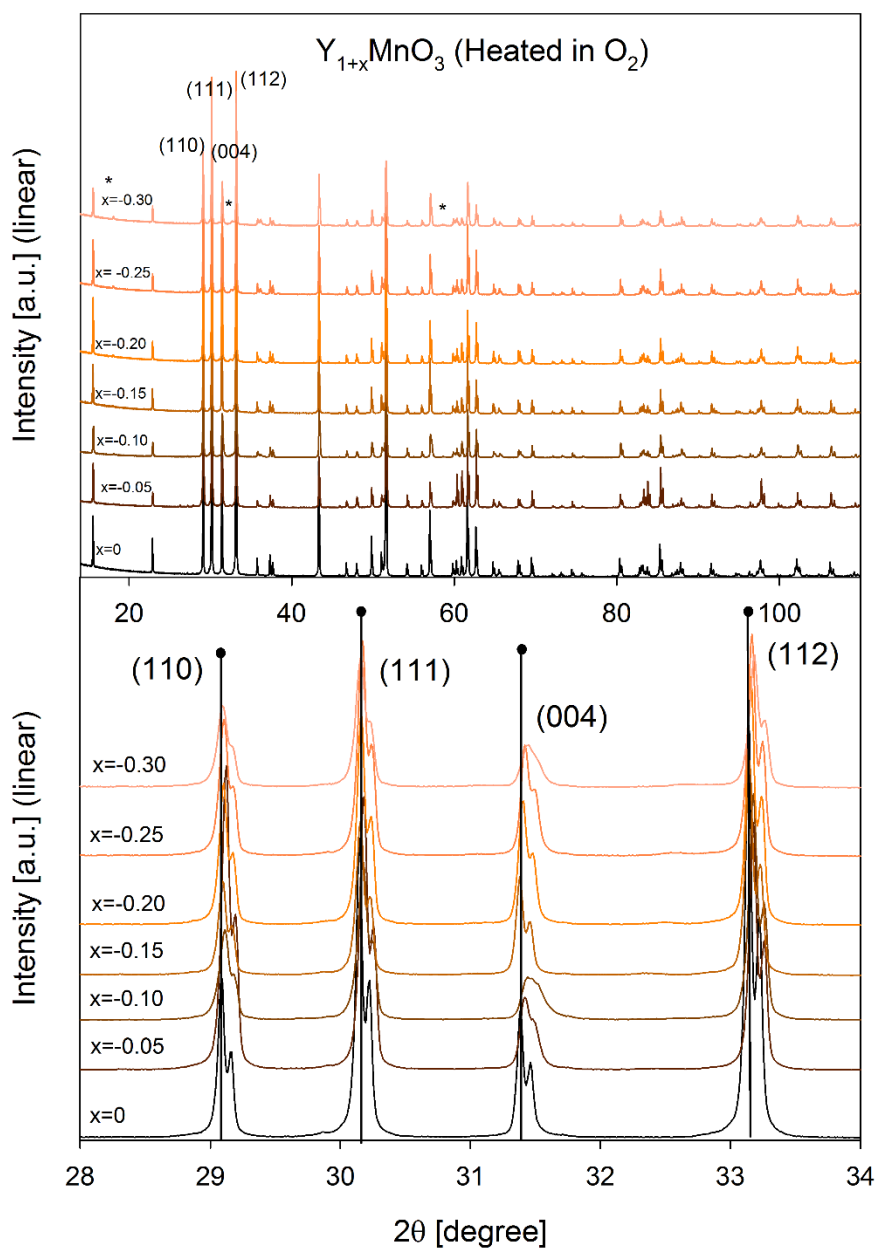


Fig. E2: X-ray diffractograms of $Y_{1+x}MnO_3$ samples with varying yttrium deficiency as prepared by solid state synthesis and heated in O_2 atmosphere. The lower end of the diagram gives a better overview of the slight shift towards higher 2θ values for the reflection belonging to (112) plane. The vertical black lines in the lower end of the diagram is a guide to the eye to see the shift of intensities better. * is indicating the pronounced intensities of Mn_3O_4 (hausmannite).

Appendix F: Temperature program of the thermogravimetric analysis of YMnO_3 and $\text{Y}_{0.80}\text{MnO}_3$.

The temperature program used during thermogravimetric analysis of YMnO_3 and $\text{Y}_{0.80}\text{MnO}_3$ made by solid state synthesis is shown in Table F1.

Tab. F1: Temperature program of the thermogravimetric analysis of YMnO_3 and $\text{Y}_{0.80}\text{MnO}_3$ made by solid state synthesis.

Step no:	Temp. init. [°C]:	Ramp [°C/min]:	Temp. end [°C]:	Dwell [min]:	Atmosphere	Flow [ml/min]:
1	30	10	1000		N_2	20-30
2	1000		1000	30	N_2	20-30
3	1000	2	500		N_2	20-30
4	500		500	15	N_2	20-30
5	500	1	30		N_2	20-30
6	30		30	15	O_2	20-30
7	30	1	500		O_2	20-30
8	500		500	15	O_2	20-30
9	500	2	1000		O_2	20-30
10	1000		1000	30	O_2	20-30
11	1000	2	500		O_2	20-30
12	500		500	15	O_2	20-30
13	500	1	30		O_2	20-30
Total analysis time:		39 h 37 min				